
Factored Diffusion Policies: Compositionally Generalized Robot Control with a Single Score Network

Sayan Mitra, Ege Yuceel, Noah Giles, Abhishek Pai
 University of Illinois Urbana-Champaign
 mitras@illinois.edu

Abstract

Robotic tasks are typically specified by a tuple of factors, such as the object to be grasped, the obstacles to be avoided, the color of the target, and so on. Collecting expert demonstrations for every combination of factor values grows combinatorially. We present *factored diffusion policies*: a single shared diffusion network trained with per-factor null-token dropout, whose score decomposes additively across factors at inference. Under approximate conditional independence between factors given the action–observation pair, this composition approximates the true joint score with a bounded uniform error, reducing the training-task budget from a product of factor cardinalities to a sum. A trajectory-tube certificate chains this score-level bound through the reverse-time sampling ODE and a contracting tracking controller into a closed-loop state-trajectory tube whose radius factors into an ODE-sensitivity constant and a per-factor score-error budget. Unlike compositional-diffusion methods for control that combine separately trained networks, we use one shared network. Drone racing experiments confirm both the generalization bound and the certificate. On state-based multi-gate racing, the factored policy passes 90% of held-out gates—matching an oracle—while a K -network composition baseline collapses to 3%; on vision-based single-gate traversal, it transfers zero-shot to an unseen venue with +11.7 pp success-rate gain and $2.4\times$ crash-rate reduction.

1 Introduction

A standard approach to robot policy learning treats the task as a monolithic input z and trains a single policy network $p(a | z)$ on a finite set of training tasks $\mathcal{Z}_{\text{train}}$ by collecting expert demonstrations for each $z \in \mathcal{Z}_{\text{train}}$. But the task usually has structure. A manipulation task is specified by the object to be grasped, its color, and the target placement pose; a locomotion task by the obstacles to be avoided and the goal; a racing task by the track geometry and the gate sizes. A task with K such factors is a tuple $z = (z_1, \dots, z_K) \in \mathcal{Z}_1 \times \dots \times \mathcal{Z}_K$, where \mathcal{Z}_i is the set of values factor i can take. Thus, the cost of monolithic conditioning grows as $\prod_i |\mathcal{Z}_i|$ even when factors vary independently.

The cost of monolithic conditioning is unavoidable in general, but it shrinks dramatically when the factors are *approximately conditionally independent given an action–observation pair* (a, o) : knowing (a, o) and the value of one factor does not appreciably help infer the others (Assumption 1). For example, for a generalizable drone racing policy, the track and the gate-opening size can be expected to be approximately conditionally independent given the drone state (o) and a planned action chunk (a) — the spatial route of the planned trajectory picks out the track while its speed and precision pick out the gate size. Under this assumption, each factor’s effect on the policy can be learned independently and combined post-hoc, dropping the training-task budget from $\prod_i |\mathcal{Z}_i|$ to $O(\sum_i |\mathcal{Z}_i|)$ and giving compositional generalization to unseen factor combinations. The remainder of the paper turns this idea into a constructive method for diffusion policies, an approximation bound, and a closed-loop certificate.

A single diffusion network with approximate conditional independence of factors. Diffusion policies are a leading method for learning control policies from expert demonstrations (Chi et al., 2023; Reuss et al., 2024): they are trained to approximate the *score* of $p(a | o, z)$, the gradient $\nabla_a \log p$ in action space. The crucial property is that density factorization under conditional independence becomes *addition* in score space, and *approximate* conditional independence becomes a bounded norm on the gradient of the residual factor interaction (Theorem 1). If the factors are approximately independent given (a, o) , then

$$\nabla_a \log p(a | o, z_1, \dots, z_K) \approx s_\emptyset + \sum_{i=1}^K \Delta_i,$$

where s_\emptyset is the unconditional score and Δ_i is the score correction for factor i alone (Definition 1). This additive composition follows from the log-density structure; in contrast, a behavior-cloning policy outputs a point estimate, and does not admit such a decomposition. We exploit additive composition by training a *single shared* score network with per-factor null-token dropout, so that each Δ_i is learned from data covering only one factor at a time, and at inference we compose $s_{\text{comp}} = s_\emptyset + \sum_i \Delta_i$ (Definition 1). This identity is the algebraic backbone of classifier-free guidance (Ho and Salimans, 2022) and compositional image generation (Liu et al., 2022; Du et al., 2023), where it composes a single concept or text-prompt factor with the unconditional score. Two things differ in our setting. First, the policy runs in closed loop: the composed score field denoises samples into actions, which a tracking controller executes on the plant, and what ultimately matters is a task-level event such as reaching a goal or gate passage. Second, we quantify the gap when conditional independence holds only approximately: Theorem 1 bounds $\|s - s_{\text{comp}}\|$ by $2\sqrt{GM}$ uniformly in z , where G bounds the residual factor-interaction strength (Assumption 1) and M bounds the curvature of the factor-interaction log-ratio. Because this bound holds for every $z \in \prod_i \mathcal{Z}_i$, including factor combinations absent from training, and s_{comp} needs only the unconditional score plus one per-factor correction, training data in which every factor value appears at least once suffices: $O(\sum_i |\mathcal{Z}_i|)$ tasks against $\Omega(\prod_i |\mathcal{Z}_i|)$ for a joint model.

Scores also make certification possible. The per-factor structure also yields a closed-loop guarantee. Fix a nominal training task z^{nom} and let the *nominal trajectory* be the closed-loop state trajectory the system would follow under the true joint score on z^{nom} . Under (i) bounded factor-interaction (Assumption 1), (ii) per-factor Lipschitz score (Assumption 3), and (iii) a contracting tracking controller (Assumption 2), the closed-loop trajectory generated by the composed policy on a (possibly held-out) test task stays within a tube of radius R around the nominal (Theorem 2). R aggregates four sources: the decomposition residual $2\sqrt{GM}$ from Theorem 1, a score-matching error $(2K - 1)\eta$ on training data, a per-factor extrapolation term and a process disturbance from sensor noise and unmodeled dynamics. The transfer from score-space to state-space error passes through an ODE-sensitivity factor C_{ode} , for which we give two computable bounds following standard methods: analytical Grönwall (uniform over tasks) and a path-dependent linear time-varying (LTV) bound using per-step Jacobians along the nominal path. If the nominal trajectory completes the task with a robustness margin of at least R , then the realized trajectory under the composed policy does so as well.

Experimental validation with drone racing. We study the approach on two drone racing settings with different factors and find the same compositional effect in both. The first, state-based full multi-gate races, uses two factors: track identity z_1 , the ordered sequence of gate positions and orientations, and gate aperture z_2 . The second, vision-based single-gate traversal, uses four factors: venue, gate color, gate ID, and approach side. Passing a gate requires the drone center to lie within the gate’s half-width r of the center at the crossing time, so the tube radius R from Theorem 2 admits the direct pass/fail comparison $R < r$. On the state-based benchmark (8 tracks \times 3 gate sizes; 6 held-out joint pairs), the factored model passes 94% of 104 gates overall and 27/30 (90%) of held-out gates, matching the oracle (95% overall, 90% held-out) and beating the unfactored baseline at 17%. The same compositional formula evaluated with 12 separately trained networks in the style of Wang et al. (2024); Mao et al. (2025) collapses to 3% on held-out gates, identifying parameter sharing rather than the additive formula as the mechanism. On the vision-based benchmark ($4 \times 3 \times 5 \times 2 = 120$ tasks), the factored model wins zero-shot transfer to a never-seen venue by +11.7 pp on success rate and $2.4\times$ on crash rate, and holds a $3.2\times$ crash-rate advantage in-distribution.

Contributions. (i) a factored diffusion policy realized as a single shared score network with per-factor null-token dropout, with a compositional generalization bound (Theorem 1) that reduces

the training-task requirement from $\Omega(\prod_i |\mathcal{Z}_i|)$ to $O(\sum_i |\mathcal{Z}_i|)$; (ii) a factored trajectory-tube certificate (Theorem 2) chaining score error through the reverse-time sampling ODE and the closed-loop tracking dynamics to a task-success criterion; (iii) empirical validation on state-based full multi-gate races and vision-based single-gate traversal (Section 4).

2 Problem of Generalizable Control from Demonstrations

Consider a robot with state $x_t \in \mathcal{X} \subseteq \mathbb{R}^n$ and discrete-time dynamics

$$x_{t+1} = f(x_t, u_t), \quad (1)$$

where $u_t \in \mathcal{U} \subseteq \mathbb{R}^m$ is the control input applied at step t . A *task* is specified by a tuple of factors $z = (z_1, \dots, z_K) \in \mathcal{Z}_1 \times \dots \times \mathcal{Z}_K$. Each task z carries a *success predicate* ϕ_z over closed-loop trajectories $x_{0:T}$ that determines whether the task is completed. We assume an expert that generates demonstration data for a finite training set $\mathcal{Z}_{\text{train}} \subsetneq \mathcal{Z}_1 \times \dots \times \mathcal{Z}_K$. The expert produces a command $a_t \in \mathcal{A}$ at each step, and a low-level *tracking controller* κ generates the final plant input $u_t = \kappa(x_t, a_t)$. We make the standard assumption that the closed-loop system formed by κ and f is contracting (Lohmiller and Slotine, 1998) or incrementally input-to-state stable (Angeli, 2002), i.e., small perturbations to a_t produce bounded state deviations (Assumption 2 in Appendix A.1). The command a_t may be a single setpoint, a trajectory, or an entire plan. At each step the policy also receives an observation $o_t \in \mathcal{O}$, which may include any subset of the robot state and a perceptual input (e.g., a camera image). The factored decomposition we develop in Section 3 is independent of the observation modality. Expert demonstrations are available only for a finite training set $\mathcal{Z}_{\text{train}}$ costing $O(|\mathcal{Z}_{\text{train}}|)$. For this paper, we assume the factors for the training tasks $z \in \mathcal{Z}_{\text{train}}$ are chosen independently randomly, that is, the training-task distribution factorizes as $p_{\text{gen}}(z) = \prod_{i=1}^K p_{\text{gen}}(z_i)$. This is a property of the data-collection protocol that holds by design. The goal is to design a policy $\pi_\theta(o_t, z)$ that generalizes from $\mathcal{Z}_{\text{train}}$ to the full product space $\mathcal{Z}_1 \times \dots \times \mathcal{Z}_K$, including tasks for which no expert demonstration or training data exists.

Running example: drone racing. In drone racing, a quadrotor has to autonomously pass through a gate using onboard IMUs and a forward-facing RGB camera. The state $x \in \mathbb{R}^{13}$ (position, attitude quaternion, velocity, body angular rate) evolves under control $u \in \mathbb{R}^4$ (collective thrust, body torque) according to Newton–Euler dynamics. We study two instantiations that share these dynamics but differ in factors and observation: a *state-based full-race* setting ($K = 2$: track \times gate-opening size, Section 4.1) and a *vision-based single-gate* setting ($K = 4$: venue, gate color, gate ID, approach side, Section 4.2). The tracking controller κ is an SE(3) geometric controller Lee et al. (2010) with fixed gains. The success predicate ϕ_z requires the drone’s center to pass within a gate half-width r of each gate center (in the case of full-race, in the prescribed order). In the state-based full-race setting, $r = r(z_2)$ varies with the gate-opening factor z_2 ; in the vision-based single-gate setting, r is fixed. Every $z \in \mathcal{Z}_{\text{train}}$ requires careful hand-tuning of the trajectory and a speed profile or training a specialized policy, or multiple expert demonstrations.

3 Approach: Compositional Generalization via Conditional Independence

Generalizing from $\mathcal{Z}_{\text{train}}$ to the full product space $\mathcal{Z} = \mathcal{Z}_1 \times \dots \times \mathcal{Z}_K$ requires additional structure: each factor’s effect on the policy must be learnable independently and combinable post hoc. The key hypothesis for our approach to work is that the factors are *approximately conditionally independent given an action–observation pair* (a, o) , that is, knowing (a, o) and the value of one factor does not help infer the others beyond what (a, o) alone reveals. For example, $z_1 = \text{track shape}$ governs the direction in a while $z_2 = \text{gate aperture}$ governs its speed — two largely disjoint channels in (a, o) , so neither factor reveals the other beyond what (a, o) already does. Formally, let $p(a, o, z)$ denote the joint distribution over action–observation–task tuples induced by the training data: sample a task $z \sim p_{\text{gen}}$, roll out the expert policy on task z , and record each action–observation pair produced along the trajectory. The forward-noising process of Section 3.1, $a_\sigma = \alpha_\sigma a + \sigma \epsilon$ with $\epsilon \sim \mathcal{N}(0, I)$ independent of (a, o, z) , extends this to a noised joint $p_\sigma(a_\sigma, o, z)$ at every $\sigma \in [0, \sigma_{\text{max}}]$, with $\sigma = 0$ recovering the clean joint. The conditional posterior $p_\sigma(z | a_\sigma, o)$ and the per-factor marginals $p_\sigma(z_i | a_\sigma, o)$ are obtained from the noised joint via Bayes’ rule. We measure the interaction among factors through the *interaction log-ratio*

$$g_\sigma(z, a_\sigma, o) := \log \frac{p_\sigma(z | a_\sigma, o)}{\prod_{i=1}^K p_\sigma(z_i | a_\sigma, o)}, \quad z = (z_1, \dots, z_K), \quad \sigma \in [0, \sigma_{\text{max}}]. \quad (2)$$

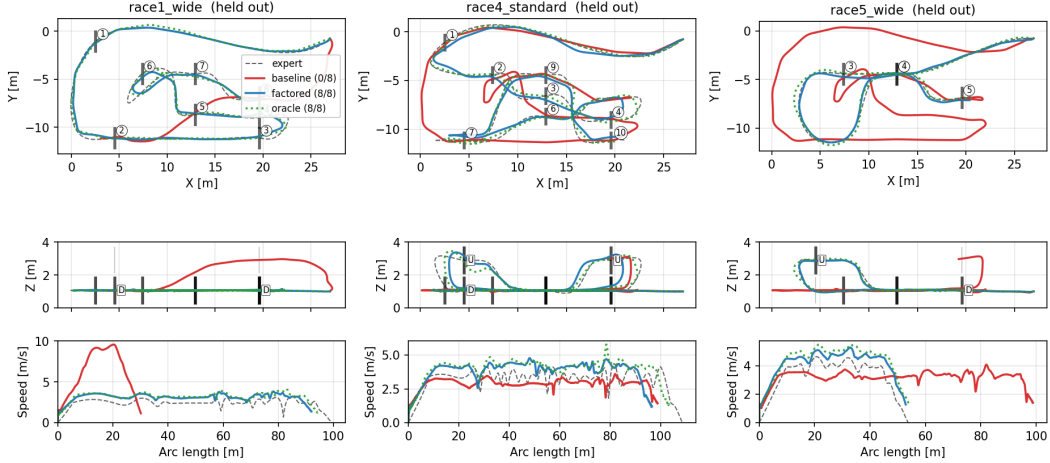


Figure 1: **Compositional generalization on held-out drone-racing tasks.** Closed-loop trajectories on three (track, gate-size) pairs not seen during training; top-down (X - Y), side view (X - Z), and speed vs. arc length. Black dashed: expert reference. Green dotted: oracle (trained on the same pair). Red: unfactored baseline. Blue: factored compositional policy $s_{\text{comp}} = s_{\varnothing} + \Delta_1 + \Delta_2$. The factored policy tracks expert and oracle to ~ 0.1 m; the baseline diverges. Aggregate over 20 tasks: Section 4.1.

Conditional independence at noise level σ holds at (a_{σ}, o) if and only if $g_{\sigma}(z, a_{\sigma}, o) = 0$ for all z .

Assumption 1 (Bounded factor interaction). There exists $G \geq 0$ such that for every noise level $\sigma \in [0, \sigma_{\max}]$, every action-observation pair (a_{σ}, o) in the support of p_{σ} , and every $z \in \mathcal{Z}_1 \times \dots \times \mathcal{Z}_K$, $|g_{\sigma}(z, a_{\sigma}, o)| \leq G$.

Even when the training prior $p_{\text{gen}}(z) = \prod_i p_{\text{gen}}(z_i)$ factorizes, conditioning on the action a can induce dependence between factors (the collider effect). It has been shown that conditional diffusion models can in general violate strict conditional independence in practice (Pal et al., 2024). Assumption 1 quantifies the strength of such effects via G . In our experiments, the residual is small empirically: the decomposition error ε_D at noised states (Table 8, mean 1.70) is an upper bound on $2\sqrt{GM}$ and is much smaller than the dominant per-factor sensitivities L_i , indicating that the factors operate on largely disjoint physical channels.

3.1 Diffusion Policies, Denoising ODEs, and ODE Sensitivity

Let $p(a | o, z)$ denote the conditional distribution over commands $a \in \mathcal{A}$ given observation o and task z , induced by the expert demonstrations. We learn to approximate $p(a | o, z)$ with a diffusion model, which operates on its *score function*, the gradient of the log-density with respect to the action. The score is the operational object on which the compositional structure can be implemented.

A diffusion model defines a forward noising process $a_{\sigma} = \alpha_{\sigma} a_0 + \sigma \epsilon$ with $\epsilon \sim \mathcal{N}(0, I)$ and $\alpha_{\sigma}^2 + \sigma^2 = 1$ ($\sigma = 0$ is clean data, large σ is near-Gaussian), where $a_0 \sim p(a | o, z)$. The score at noise level σ is

$$s(a_{\sigma}, \sigma, o, z) := \nabla_{a_{\sigma}} \log p_{\sigma}(a_{\sigma} | o, z), \quad (3)$$

where p_{σ} is the marginal density of a_{σ} . A neural network s_{θ} approximates s via denoising score matching. Actions are generated by solving the reverse sampling ODE

$$\frac{da_{\sigma}}{d\sigma} = f_{\text{dr}}(\sigma) a_{\sigma} + \tilde{g}(\sigma) s_{\theta}(a_{\sigma}, \sigma, o, z) \quad (4)$$

backward from σ_{\max} (near-Gaussian) to $\sigma \approx 0$ (near-clean), where f_{dr} and \tilde{g} are schedule-dependent drift and diffusion coefficients. In practice the integration is performed with a discrete-time scheduler such as DDIM (Denoising Diffusion Implicit Models Song et al., 2021a), which under a deterministic-seed setting realizes (4). At inference on an unseen task the policy runs a *composed learned* score that differs from the true joint score, and we need to bound how much this difference affects the generated command. The bound below is a standard application of Grönwall’s inequality to (4); similar arguments appear in convergence analyses for diffusion samplers (Song et al., 2021b; Chen

et al., 2023; Benton et al., 2024). Before stating it, we fix one mild setup choice: throughout the sensitivity analysis, both denoising chains are run from a shared initial sample $a_{\sigma_{\max}} = a'_{\sigma_{\max}} = a^*$. Since (4) is a probability-flow ODE, fixing the seed makes the sampled action a deterministic function of (o, z) and yields a per-task certificate without quantifying over the Gaussian cover. Section 4.1 verifies that the conclusions transfer to fresh-seed-per-rollout sampling at deployment.

Lemma 1 (ODE Sensitivity). *Let $s, s' : \mathcal{A} \times [0, \sigma_{\max}] \rightarrow \mathcal{A}$ be two score fields with (a) $\|s - s'\|_{\infty} \leq \varepsilon$ and (b) s is $L_a(\sigma)$ -Lipschitz in its first argument. Let $\{a_{\sigma}\}, \{a'_{\sigma}\}$ be denoising paths generated by the reverse ODE (4) from a shared initial noise $a_{\sigma_{\max}} = a'_{\sigma_{\max}}$. Then*

$$\|a_0 - a'_0\| \leq C_{\text{ode}} \cdot \varepsilon, \quad C_{\text{ode}} := \int_0^{\sigma_{\max}} |\tilde{g}(\sigma)| \exp\left(\int_0^{\sigma} [|f_{\text{dr}}(\sigma')| + |\tilde{g}(\sigma')| L_a(\sigma')] d\sigma'\right) d\sigma. \quad (5)$$

Lemma 1 is conservative: the scalar Lipschitz bound $L_a(\sigma)$ collapses all directional structure of the score Jacobian, and the Grönwall integral compounds the worst case at every noise level. Both losses are recoverable. Linearizing the discrete DDIM map (4) around the nominal denoising trajectory $\{\bar{a}_k\}$ yields a discrete state-transition matrix $\Phi_{k+1, K}$ whose operator norm replaces the scalar Lipschitz product, capturing both the anisotropy of the per-step Jacobians $J_k = \partial s / \partial a|_{\bar{a}_k}$ and inter-step cancellation of worst-case directions Fan et al. (2016). The resulting *path-dependent LTV* constant $C_{\text{ode}}^{\text{LTV}}(\bar{a})$ (Lemma 2) is typically 5 orders of magnitude tighter than the Grönwall constant on our experiments (Section 4.1).

3.2 Factored Score Decomposition

Definition 1 (Composed score). Let $z = (z_1, \dots, z_K)$ be a task. For each $i \in \{1, \dots, K\}$, the *score correction* for factor i is $\Delta_i(a_{\sigma}, \sigma, o, z_i) = s(a_{\sigma}, \sigma, o, z_i) - s(a_{\sigma}, \sigma, o)$, where $s(\cdot, z_i)$ is the score conditioned on factor i alone (other factors marginalized via null-token substitution) and $s(\cdot)$ is fully unconditional. The *composed score* for z is

$$s_{\text{comp}}(a_{\sigma}, \sigma, o, z) = s(a_{\sigma}, \sigma, o) + \sum_{i=1}^K \Delta_i(a_{\sigma}, \sigma, o, z_i). \quad (6)$$

Theorem 1 (Decomposition error bound). *Suppose Assumption 1 holds and for every $\sigma \in [0, \sigma_{\max}]$, the interaction log-ratio g_{σ} defined in (2) is twice differentiable in a_{σ} with $\|\nabla_{a_{\sigma}}^2 g_{\sigma}(z, a_{\sigma}, o)\|_{\text{op}} \leq M$ uniformly in σ, a_{σ}, o, z . Then for all a_{σ}, σ, o, z ,*

$$\|s(a_{\sigma}, \sigma, o, z) - s_{\text{comp}}(a_{\sigma}, \sigma, o, z)\| \leq 2\sqrt{GM}. \quad (7)$$

The composed score s_{comp} approximates the true joint score $s(\cdot, z)$ within $2\sqrt{GM}$ for every $z \in \mathcal{Z}_1 \times \dots \times \mathcal{Z}_K$, including tuples absent from $\mathcal{Z}_{\text{train}}$. Computing s_{comp} requires $K + 1$ learned components (Definition 1): the unconditional score $s(\cdot)$ and one per-factor score $s(\cdot, z_i)$ for each factor i . Learning $s(\cdot, z_i)$ requires training data in which the value z_i appears with at least one setting of the other factors. A training set of size $|\mathcal{Z}_{\text{train}}| = O(\sum_i |\mathcal{Z}_i|)$ in which every factor value appears in at least one training task therefore suffices to evaluate s_{comp} on all $\prod_i |\mathcal{Z}_i|$ tasks. A joint (non-compositional) model that learns $s(\cdot, z)$ directly requires $\Omega(\prod_i |\mathcal{Z}_i|)$ demonstrations.

The decomposition $s_{\text{comp}} = s + \sum_i \Delta_i$ is not fully determined by training data: a constant can shift between s and any Δ_i without changing s_{comp} . We resolve this via *factor dropout* during training, replacing each factor conditioning independently with a learned null token with probability p_{drop} , so s is identified as the all-null behavior and each Δ_i as the residual when only factor i is revealed (Appendix A.3).

3.3 Trajectory Tube Certificate

In our setting the expert controller is deterministic: for each (o, z) there is a unique reference chunk $a_0^*(o, z) \in \mathcal{A}$, so $p(a_0 | o, z) = \delta(a_0 - a_0^*(o, z))$, where δ denotes the Dirac delta distribution (a point mass at a_0^*). The noised density is then a Gaussian centered at $\alpha_{\sigma} a_0^*$, and the true score has the closed form $s(a_{\sigma}, \sigma, o, z) = -\frac{a_{\sigma} - \alpha_{\sigma} a_0^*(o, z)}{\sigma^2}$. This closed form makes the score-matching error η (8) directly measurable from training data.

Theorem 2 additionally needs a per-factor Lipschitz regularity of the trained score with respect to each factor z_i (Assumption 3); this is a mild architectural property that supplies the per-factor sensitivity constants L_i . The remaining ingredient is the network’s approximation error. The score-matching error η is a *measured* quantity: the worst-case gap between s_θ and the true score on the training set,

$$\eta := \sup_{\substack{a_\sigma, \sigma, o \\ c \in \mathcal{Z}_{\text{train}} \cup \{\emptyset\}}} \|s_\theta(a_\sigma, \sigma, o, c) - s(a_\sigma, \sigma, o, c)\|, \quad (8)$$

where c ranges over all conditioning configurations used in the composed score (unconditional, each single-factor, and the joint). The denoising score-matching training loss is an unbiased estimate of the *expected* squared score error $\mathbb{E}[\|s_\theta - s\|^2]$ (Song et al., 2021b), which by Jensen’s inequality lower-bounds η^2 . Empirical sup-bounds on η are obtained by worst-case sampling over noised states drawn along the nominal denoising trajectory; the per-combo $\varepsilon_s^{(z)} := \max_k \|\Delta \varepsilon_k^{(z)}\|$ measurements reported in Appendix B.9 are the operational instantiation of this estimate. A small training loss is necessary but not sufficient for small η . Expanding the composed score (Definition 1) gives $s^{\text{comp}} = \sum_{i=1}^K s(\cdot, z_i) - (K-1)s_{\emptyset}$, i.e., the unconditional baseline appears with coefficient $-(K-1)$. The triangle inequality on $s_\theta^{\text{comp}} - s^{\text{comp}}$ therefore gives $K\eta + (K-1)\eta = (2K-1)\eta$:

$$\|s_\theta^{\text{comp}} - s^{\text{comp}}\| \leq (2K-1)\eta. \quad (9)$$

Theorem 2 (Factored trajectory tube). *Under Assumptions 1, 2, and 3, and either (a) the $L_a(\sigma)$ -Lipschitz condition of Lemma 1, or (b) the Jacobian regularity of Lemma 2, let x_t^{nom} be the closed-loop state trajectory under the true joint score $s(\cdot, z^{\text{nom}})$ for a nominal task $z^{\text{nom}} \in \mathcal{Z}_{\text{train}}$, and let x_t be the trajectory under the composed learned score $s_\theta^{\text{comp}}(\cdot, z)$ with per-factor perturbations $\|z_i - z_i^{\text{nom}}\| \leq \delta_i$ for each $i \in \{1, \dots, K\}$, starting from $\|x_0 - x_0^{\text{nom}}\| \leq \delta_0$. Let η be the score-matching error (8), measured on $\mathcal{Z}_{\text{train}}$. Then*

$$\|x_t - x_t^{\text{nom}}\| \leq \lambda^t \delta_0 + \frac{B_\kappa C_{\text{ode}} \varepsilon_s + w}{1 - \lambda}, \quad (10)$$

where the total score perturbation decomposes as $\varepsilon_s \leq 2\sqrt{GM} + (2K-1)\eta + \sum_{i=1}^K L_i \delta_i$, with terms from Theorem 1, the network approximation error (9), and the factor perturbation.

C_{ode} is instantiated either by the Grönwall bound $C_{\text{ode}}^{\text{ana}}$ (Lemma 1, uniform over z) or by the path-dependent LTV bound $C_{\text{ode}}^{\text{LTV}}(\bar{a}^{(z)})$ (Lemma 2, per-task). Under hypothesis (a) the bound (10) is a strict upper bound on the closed-loop state error. Under hypothesis (b) it is first-order in ε_s , with an $O(\varepsilon_s^2)$ Taylor remainder propagates additively through the contraction proof; the remainder is controlled when $\varepsilon_s \cdot C_{\text{ode}}^{\text{LTV}}$ is small relative to the local radius of linearization (Remark 3), which is within a margin of $\sim 10\times$ for the full race experiments (Section 4.1).

Corollary 1. *After the transient $\lambda^t \delta_0$ decays the closed-loop state error satisfies $\|x_t - x_t^{\text{nom}}\| \leq R_{\text{ss}}$ with C_{ode} from Theorem 2 and $R_{\text{ss}} = (B_\kappa C_{\text{ode}} \varepsilon_s + w)/(1 - \lambda)$.*

The factored bound $\sum_i L_i \delta_i$ replaces the joint bound $L_{\text{joint}} \|\delta\|$ with a per-factor weighted sum. Neither is uniformly tighter; the factored certificate beats the joint certificate when $2\sqrt{GM} + \sum_i L_i \delta_i < L_{\text{joint}} \|\delta\|$, a condition on both the factor-interaction strength and the alignment of δ with the dominant Lipschitz directions (Appendix D).

For the drone-racing experiments, the trajectory tube specializes to a per-gate passage criterion. Define the worst-case tube radius $R = \delta_0 + R_{\text{ss}}$; then Theorem 2 delivers gate passage as follows: if the nominal trajectory x_t^{nom} passes through every gate center exactly ($p_{t_g}^{\text{nom}} = c_g$ at each crossing time t_g , $g = 1, \dots, G$) and $R < r(z_2)$, then $\|p_{t_g} - c_g\| < r(z_2)$ for every gate on the trajectory generated by the composed learned score, i.e., gate passage is guaranteed. The gate-size factor z_2 controls R through Δ_2 (slowing the drone near narrow gates) and sets the threshold $r(z_2)$ (wider gates are easier to certify). The *certifiable region* $\{z_2 \in \mathcal{Z}_2 : r(z_2) > R\}$ grows as the score-perturbation budget ε_s shrinks, i.e., as the decomposition residual $2\sqrt{GM}$ and the score-matching error η both decrease (factors closer to conditional independence and a better-trained network).

4 Experiments: Agile Aerial Robotics

Drone racing is a demanding benchmark for generalizable control: visual venue, gate color, track geometry, gate-opening size, and approach side can all be varied independently, spanning both

appearance and *geometry+dynamics*. In practice each track is a separate engineering problem; competition teams spend days to weeks per configuration (Kaufmann et al., 2023; Song et al., 2023), and joint generalization across these axes is not standard. Section 4.2 (vision) holds out a visually distinct venue; Section 4.1 (state) holds out unseen track \times gate-size pairs.

All our runs use a 0.5 kg, 25 cm racing-class quadrotor, simulated as a 6-DOF Newton–Euler rigid body at 600 Hz. Three diffusion policies differing only in factor conditioning: *Baseline* (no factor input); *Factored* (ours: per-factor embeddings with $p_{\text{drop}}=0.1$ null-token dropout; composed score $s_{\text{comp}}=s_{\emptyset} + \sum_i \Delta_i$, Definition 1); *Oracle* (factored, trained on all tasks including held-out — architectural upper bound). Baseline and Factored are trained only on held-in tasks.

4.1 State-Based Full-Race Composition

The quadrotor must complete full multi-gate races (2–10 gates per track) using state-based control. The diffusion model generates a trajectory of $K = 32$ keypoints $a^j = (p_j, v_{\text{speed},j}) \in \mathbb{R}^4$ per task; at inference, keypoints are linearly interpolated to $N = 256$ dense waypoints (velocity from unit tangent \times speed; yaw from $\text{atan2}(v_y, v_x)$) and tracked by the low-level SE(3) controller. Eight race tracks (race1–8) share a common gate layout but different gate sequences. Two factors define a task: track identity $z_1 \in \{\text{race1}, \dots, \text{race8}\}$ and gate-opening size $z_2 \in \{\text{narrow } (r=0.3 \text{ m}), \text{standard } (0.762 \text{ m}), \text{wide } (1.0 \text{ m})\}$. The two factors are approximately conditionally independent: z_1 sets the geometric raceline, while z_2 primarily modulates the speed profile along that path (narrower gates demand slower passage). Of $8 \times 3 = 24$ tasks, 20 are feasible; per-task max feasible speed is found by binary search. The denoiser is a 1D temporal ConvNet (4.3M parameters) with Emb(8, 64) for track and Emb(3, 64) for gate-size, each with a learned null token, trained from 50 DAgger-style rollouts per task. Six (track, gate-size) pairs are held out from training: (race1, wide), (race4, standard), (race5, wide), (race6, narrow), (race7, standard), (race8, wide). Every factor level appears in ≥ 5 training tasks; only the joint pairs are unseen. Track descriptions, the speed maps, per-task results, ablations, and certificate results appear in Appendix B.

Main results. Table 1 reports closed-loop gate passage across all 20 feasible tasks (104 gates total), broken down by training (74 gates over 14 tasks) and held-out (30 gates over 6 tasks). The factored model with composed inference reaches 94% on the full task set, within one gate of the oracle (95%), and recovers 27/30 (90%) of held-out gates — matching the oracle exactly without any training data on those joint pairs (Figure 1). The single held-out failure is (race6, narrow), which the oracle also fails (0/3 even with direct training data): the trained policy generates 3.4 m/s for race6 (reference: 2.4 m/s), at the edge of the SE(3) controller’s ability to track slow speeds through race6’s geometry. Since oracle fails this combo despite direct training, the limit is a control / network-capacity constraint rather than a composition error.

Table 1: Gate passage on full multi-gate races. Both *Factored* and the K -network baseline use the same composition formula at inference and differ only in whether one shared network or $K = 12$ separately trained networks evaluate the formula.

Method	All (104)	Training (74)	Held-out (30)	Crashes
Baseline (no factor)	33/104 (32%)	28/74 (38%)	5/30 (17%)	0
K -network composition (12)	50/104 (48%)	49/74 (66%)	1/30 (3%)	2
Factored, composed (ours)	98/104 (94%)	71/74 (96%)	27/30 (90%)	0
Oracle (factored, all data)	99/104 (95%)	72/74 (97%)	27/30 (90%)	0

Sharing parameters across factors is the mechanism. Reading Table 1 along the second and third rows isolates the architectural finding: the K -network baseline uses an identical composition formula with $K = 12$ separately trained unconditional networks (ε_{\emptyset} trained on all held-in tasks pooled, plus eight track-only and three gate-size-only networks), and collapses to 3% on held-out tasks (30 \times ratio). It also fails on *training* tasks that have only one feasible held-in gate size — race1_standard (0/8) and race4_wide (0/10) — because the per-track network collapses onto its single training raceline and the per-gate correction does not consistently steer it back to the joint trajectory. The compositional formula alone is not enough; sharing parameters across factors during training is what makes the additive composition work. Full K -network details are in Appendix B.6.

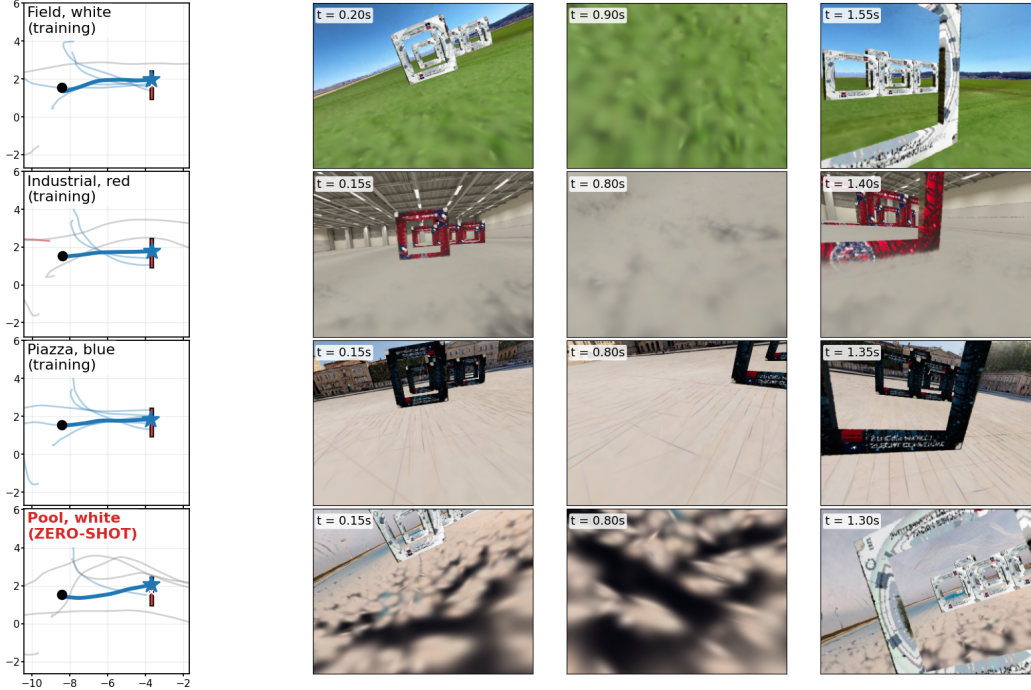


Figure 2: **Zero-shot venue transfer.** Each row shows the policy on a different (venue, gate-color) pair: Field–white, industrial–red, piazza–blue, and pool–white (*zero-shot*). Pool is entirely excluded from training; the policy never observes pool’s photometric distribution (water, sky reflections), yet passes its gate (filled rectangle) from a single onboard RGB camera and a noisy gyro. *Left*: bird’s-eye view of rollouts. Bold blue line = highlighted successful rollout (camera frames in that row are taken from this trajectory); thin blue = other successes; gray = timeouts; red = crashes. *Right*: three onboard camera chronological frames along the highlighted rollout.

Certificates. We instantiate Theorem 2 with the path-dependent LTV sensitivity of Lemma 2, obtaining finite task-wise sensitivity bounds that are six orders of magnitude tighter than the uniform Grönwall bound. The resulting norm-based tubes remain conservative relative to the physical gate margins, so we treat them as a robustness diagnostic rather than a deployment-level certificate. Further details on empirical measurements and residual-gap analysis are in Appendix B.

4.2 Vision-Based Single-Gate Traversal

The quadrotor must fly through a single race gate from diverse spawn positions (3–10 m range, $\pm 45^\circ$ azimuth, both approach sides) using only an onboard 320×240 RGB camera and a noisy gyro. The diffusion network predicts a chunk of $T = 16$ future body-frame offsets to the target gate; the first prediction is converted to a world-frame position estimate via the known gate location and gyro-integrated orientation, then tracked by the soft-preset SE(3) controller of Section 4. The visual encoder is a ResNet-18 with the last two blocks fine-tuned (13.9M trainable parameters). Four factors span the task space: *venue* (4: Field, industrial, piazza, pool), *gate color* (3), *gate ID* (5), and *approach side* (± 1), for $4 \cdot 3 \cdot 5 \cdot 2 = 120$ tasks. We evaluate compositional generalization along two axes: *within-venue* (held-out (color, gate, side) triples in seen venues, interpolation in the factor product) and *zero-shot venue transfer* (an entire venue held out, extrapolation across visual domain), comparing the three models defined in Section 4 (Baseline, Factored, Oracle).

Main results. Pool, visually the most distinct venue (water, reflections, sky), is held out entirely; both models train on Field + industrial + piazza (8,550 rollouts) and evaluate zero-shot on pool. Within-venue compositional generalization (Table 2, right) shows only a modest factored advantage: +1.1 pp on held-out (color, gate, side) triples and +2 pp on training combos. After two DAGger rounds both models exceed 58% on the small per-venue product space ($3 \times 5 \times 2 = 30$ combinations); the encoder has already adapted to each venue’s photometry and the geometry signal generalizes

across held-out triples on its own, leaving little room for the factor decomposition to help. The story changes under zero-shot venue transfer (Table 2, left): on pool, the factored model wins by +11.7 pp on success rate and $2.4\times$ on crash rate. Even in simulation this is surprising: a deep visual encoder driving a control policy through a never-seen photometric distribution is not a default outcome, and a real-world analog (a drone racing through a new venue with only a single onboard camera) would go beyond current systems. The crash-rate advantage is the a durable signal: $3.2\times$ in-distribution, $2.4\times$ zero-shot even as the within-venue success-rate gap narrows to ~ 1 pp. We attribute this to the factored composition: the venue embedding captures appearance while the gate, color, and side embeddings carry geometry; under photometric distribution shift the geometric channel is preserved and failures become soft (timeouts, near-misses) rather than hard (collisions).

Table 2: Vision-based single-gate results. *Left*: zero-shot venue transfer (pool held out; three train venues shown as in-distribution sanity check; success / (crash) across n trials). *Right*: within-venue compositional generalization at higher accuracy (All 4 venues, 25 held-out (color, gate, side) combos).

Model	3 train ($n=180$)	Pool 0-shot ($n=120$)	Model	Train	Held-out	Crash
Baseline	41.7% (34.4%)	25.0% (36.7%)	Baseline	67.8%	58.3%	18.5%
Factored	63.3% (10.6%)	36.7% (15.0%)	Factored	69.8%	59.4%	14.0%
Adv.	+21.6 pp / $3.2\times$	+11.7 pp / $2.4\times$				

Certificates. We apply the same path-dependent LTV machinery as Section 4.1 (per-step DDIM Jacobians along the deterministic reverse path, backward Lyapunov recursion $P_s = M_s^\top P_{s+1} M_s$, $C_{\text{ode}}^{\text{LTV}} = \sum_s |c_2(s)| \sqrt{\|P_{s+1}\|}$). In this setting (DDIM 10), $C_{\text{ode}}^{\text{LTV}}$ is tightly clustered (mean 2074, range 2057–2088 across 18 within-distribution combos) and $\varepsilon_s \approx 1.95$, giving $R_{\text{ss}} \approx 2,023$ m. Unlike the full race experiment of the previous section, here the the LTV bound does *not* get close to the empirical gap and this is not a particularly useful certificate.

5 Related Work

Diffusion Policy (Chi et al., 2023) and its multi-task, 3D, and flow-matching extensions (Reuss et al., 2024; Ze et al., 2024; Black et al., 2024) treat task variation as a monolithic conditioning input. Compositional diffusion in image generation (Liu et al., 2022; Du et al., 2023; Ho and Salimans, 2022; Wang et al., 2023) established the additive score identity we adapt to control. Several recent works also compose diffusion policies for robotics, each on a different compositional axis: heterogeneous data sources (PoCo, Wang et al., 2024), test-time policy mixtures (GPC, Cao et al., 2026), latent behavioral modes (FDP, Liu et al., 2025), input modalities (Modality-Composable DP, Cao et al., 2025), or track-specific networks (Mao et al., 2025). All combine K separately trained networks at inference; we use a single shared score network with per-factor null-token dropout, named factors with held-out combination generalization, and a closed-loop trajectory-tube certificate.

Certified-robustness frameworks (Fazlyab et al., 2019; Everett et al., 2021; Astorga et al., 2023) treat the policy monolithically; sequential skill composition (Liang et al., 2024; Mishra et al., 2023) operates across time rather than across factors; champion-level drone racing (Kaufmann et al., 2023; Song et al., 2023; Foehn et al., 2021) tunes per track; domain randomization (Tobin et al., 2017; Sadeghi and Levine, 2017) and task-conditioned multi-task RL randomize or condition over factors at training without explicit per-factor composition. Extended discussions are in Appendix E.

6 Limitations and Broader Impacts

The trajectory-tube certificate of Section 3.3 closes for the state-based full-race policy but does not transfer to the vision-based single-gate policy: a gap that is structural to operator-norm path analysis on image-conditioned scores. Closing it likely requires a non-norm-based, manifold-aware sensitivity analysis which we leave to future work. Full vision-based multi-gate races are a longer-term direction. Beyond certificates, they raise challenges in generalizability even with an oracle action policy.

Sample-efficient autonomous-flight policies have potential positive applications (inspection, search-and-rescue, delivery) and dual-use risks (surveillance, weaponised UAVs) common to autonomous-aviation research. Standard deployment-stage mitigations (geofencing, operator authentication, regulatory compliance) apply but are out of scope for this simulation-only certificate paper.

Acknowledgments and Disclosure of Funding

References

- David Angeli. A Lyapunov approach to incremental stability properties. *IEEE Transactions on Automatic Control*, 47(3):410–421, 2002.
- Angello Astorga, Chiao Hsieh, P. Madhusudan, and Sayan Mitra. Perception contracts for safety of ml-enabled systems. *Proc. ACM Program. Lang.*, 7(OOPSLA2), October 2023. doi: 10.1145/3622875. URL <https://doi.org/10.1145/3622875>.
- Joe Benton, Valentin De Bortoli, Arnaud Doucet, and George Deligiannidis. Nearly d -linear convergence bounds for diffusion models via stochastic localization. In *International Conference on Learning Representations (ICLR)*, 2024.
- Kevin Black, Noah Brown, Danny Driess, Adnan Esmail, Michael Equi, Chelsea Finn, Niccolo Fusai, Lachy Groom, Karol Hausman, Brian Ichter, et al. π_0 : A vision-language-action flow model for general robot control. *arXiv preprint arXiv:2410.24164*, 2024.
- Yongyuan Cao, Qian Zhang, et al. Modality-composable diffusion policy via inference-time distribution-level composition. *arXiv preprint arXiv:2503.12466*, 2025.
- Yongyuan Cao et al. Compose your policies! improving diffusion-based or flow-based robot policies via test-time distribution-level composition. In *International Conference on Learning Representations (ICLR)*, 2026. To appear.
- Sitan Chen, Sinho Chewi, Jerry Li, Yuanzhi Li, Adil Salim, and Anru R. Zhang. Sampling is as easy as learning the score: Theory for diffusion models with minimal data assumptions. In *International Conference on Learning Representations (ICLR)*, 2023.
- Cheng Chi, Siyuan Feng, Yilun Du, Zhenjia Xu, Eric Cousineau, Benjamin Burchfiel, and Shuran Song. Diffusion policy: Visuomotor policy learning via action diffusion. In *Robotics: Science and Systems (RSS)*, 2023.
- Yilun Du, Conor Durkan, Robin Strudel, Joshua B. Tenenbaum, Sander Dieleman, Rob Fergus, Jascha Sohl-Dickstein, Arnaud Doucet, and Will Grathwohl. Reduce, reuse, recycle: Compositional generation with energy-based diffusion models and MCMC. In *International Conference on Machine Learning (ICML)*, 2023.
- Michael Everett, Golnaz Habibi, Chuangchuang Sun, and Jonathan P. How. Reachability analysis of neural feedback loops. *IEEE Access*, 9:163938–163953, 2021.
- Chuchu Fan, James Kapinski, Xiaoqing Jin, and Sayan Mitra. Locally optimal reach set over-approximation for nonlinear systems. In *Proceedings of the 13th ACM-SIGBED International Conference on Embedded Software (EMSOFT)*, EMSOFT '16, pages 6:1–6:10, New York, NY, USA, 2016. ACM. URL <http://doi.acm.org/10.1145/2968478.2968482>. Nominated for best paper award.
- Mahyar Fazlyab, Alexander Robey, Hamed Hassani, Manfred Morari, and George J. Pappas. *Efficient and accurate estimation of lipschitz constants for deep neural networks*. Curran Associates Inc., Red Hook, NY, USA, 2019.
- Philipp Foehn, Angel Romero, and Davide Scaramuzza. Time-optimal planning for quadrotor waypoint flight. *Science Robotics*, 6(56), 2021.
- Jonathan Ho and Tim Salimans. Classifier-free diffusion guidance. In *NeurIPS Workshop on Deep Generative Models and Downstream Applications*, 2022.
- Yifei Ji et al. Compositional perception contracts for verified autonomy. *arXiv preprint*, 2025.
- Elia Kaufmann, Leonard Bauersfeld, Antonio Loquercio, Matthias Müller, Vladlen Koltun, and Davide Scaramuzza. Champion-level drone racing using deep reinforcement learning. *Nature*, 620:982–987, 2023.
- Taeyoung Lee, Melvin Leok, and N. Harris McClamroch. Geometric tracking control of a quadrotor UAV on SE(3). In *IEEE Conference on Decision and Control (CDC)*, 2010.
- Zhixuan Liang, Yao Mu, Hengbo Ma, Masayoshi Tomizuka, Mingyu Ding, and Ping Luo. SkillDiffuser: Interpretable hierarchical planning via skill abstractions in diffusion-based task execution. In *IEEE/CVF Conference on Computer Vision and Pattern Recognition (CVPR)*, 2024.

- Hanzhe Liu, Jia Chen, Sebastian Høeg, Yuxuan Yao, Yifan Li, Kris Hauser, and Yilun Du. Flexible multitask learning with factorized diffusion policy. *arXiv preprint arXiv:2512.21898*, 2025.
- Nan Liu, Shuang Li, Yilun Du, Antonio Torralba, and Joshua B. Tenenbaum. Compositional visual generation with composable diffusion models. In *European Conference on Computer Vision (ECCV)*, 2022.
- Winfried Lohmiller and Jean-Jacques E. Slotine. On contraction analysis for non-linear systems. *Automatica*, 34(6):683–696, 1998.
- Han Mao et al. Composing diffusion policies for few-shot learning of trajectory generation in autonomous racing. *arXiv preprint 2410.17479v1*, 2025.
- Utkarsh A. Mishra, Shangjie Xue, Yongxin Chen, and Danfei Xu. Generative skill chaining: Long-horizon skill planning with diffusion models. In *Conference on Robot Learning (CoRL)*, 2023.
- Sachit Pal et al. CoInD: Enabling logical compositions in diffusion models. *arXiv preprint*, 2024. Please verify exact author list, arXiv ID, and venue.
- Moritz Reuss, Ömer Erdinç Yagmurlu, Fabian Wenzel, and Rudolf Lioutikov. Multimodal diffusion transformer: Learning versatile behavior from multimodal goals. In *Robotics: Science and Systems (RSS)*, 2024.
- Fereshteh Sadeghi and Sergey Levine. CAD²RL: Real single-image flight without a single real image. In *Robotics: Science and Systems (RSS)*, 2017.
- Jiaming Song, Chenlin Meng, and Stefano Ermon. Denoising diffusion implicit models. In *International Conference on Learning Representations (ICLR)*, 2021a.
- Yang Song, Jascha Sohl-Dickstein, Diederik P. Kingma, Abhishek Kumar, Stefano Ermon, and Ben Poole. Score-based generative modeling through stochastic differential equations. In *International Conference on Learning Representations (ICLR)*, 2021b.
- Yunlong Song, Angel Romero, Matthias Müller, Vladlen Koltun, and Davide Scaramuzza. Reaching the limit in autonomous racing: Optimal control versus reinforcement learning. *Science Robotics*, 8(82), 2023.
- Joshua Tobin, Rachel Fong, Alex Ray, Jonas Schneider, Wojciech Zaremba, and Pieter Abbeel. Domain randomization for transferring deep neural networks from simulation to the real world. In *IEEE/RSJ International Conference on Intelligent Robots and Systems (IROS)*, 2017.
- Lirui Wang, Jialiang Zhao, Yilun Du, Edward H. Adelson, and Russ Tedrake. PoCo: Policy composition from and for heterogeneous robot learning. In *Robotics: Science and Systems (RSS)*, 2024.
- Zihao Wang, Lin Gui, Jeffrey Negrea, and Victor Veitch. Concept algebra for (score-based) text-controlled generative models. In *Advances in Neural Information Processing Systems (NeurIPS)*, 2023.
- Yanjie Ze, Gu Zhang, Kangning Zhang, Chenyuan Hu, Muhan Wang, and Huazhe Xu. 3D diffusion policy: Generalizable visuomotor policy learning via simple 3D representations. In *Robotics: Science and Systems (RSS)*, 2024.

A Formal Assumptions and Proofs

This appendix collects the full formal statement of the cascade-contraction assumption and the proofs of all results stated in the main paper. Each result is restated for self-containedness; numbering refers to the main-paper labels.

A.1 Cascade contraction assumption

Assumption 2 (Cascade contraction). The closed-loop system consisting of the tracking controller κ and the plant dynamics f is contracting: for any two command sequences $\{a_t\}$ and $\{a'_t\}$ and corresponding state trajectories $\{x_t\}$ and $\{x'_t\}$ satisfying $x_{t+1} = f(x_t, \kappa(x_t, a_t))$,

$$\|x_{t+1} - x'_{t+1}\| \leq \lambda \|x_t - x'_t\| + B_\kappa \|a_t - a'_t\| + w, \quad (11)$$

where $\lambda \in [0, 1)$ is the per-step contraction rate, $B_\kappa > 0$ is the command-to-state gain, and $w \geq 0$ is the per-step disturbance from sensor noise and unmodeled dynamics.

This assumption is a property of the tracking controller and plant, independent of how the commands a_t are generated (by a diffusion policy, a hand-tuned planner, or any other source). Contraction ensures that state deviations caused by command perturbations remain bounded rather than accumulating over time. On its own, contraction does not yield a useful certificate: it bounds state deviation in terms of *command* perturbation $\|a_t - a'_t\|$, but says nothing about how large that perturbation is or how it depends on the task. The factored diffusion policy fills this gap by decomposing the command perturbation into per-factor contributions $\sum L_i \delta_i$, each of which can be bounded independently. The certificate (Theorem 2) chains the two: factorization controls the commands, contraction propagates commands to states.

A.2 Per-factor Lipschitz score

Assumption 3 (Per-factor Lipschitz score). For each factor $i \in \{1, \dots, K\}$,

$$\|s_\theta(\cdot, z_i) - s_\theta(\cdot, z'_i)\| \leq L_i \|z_i - z'_i\| \quad (12)$$

for all $z_i, z'_i \in \mathcal{Z}_i$ and all (a_σ, σ, o) , where L_i is the Lipschitz constant of the i -th conditioning branch.

This is a mild regularity property of the trained network rather than a substantive task hypothesis. For finite discrete factor spaces \mathcal{Z}_i (such as the eight tracks and three gate-opening sizes used in our experiments) the right-hand side of (12) is automatically finite: L_i is the maximum-over-pairs ratio $\max_{z_i \neq z'_i} \|s_\theta(\cdot, z_i) - s_\theta(\cdot, z'_i)\| / \|z_i - z'_i\|$ and is computed exactly by evaluating all factor pairs. For continuous factor spaces the bound follows from the network architecture: each z_i enters the network through a learned embedding followed by Lipschitz operations (linear layers with bounded weights, layer normalization, and standard nonlinearities), whose composition is Lipschitz in the input. What matters operationally is the *magnitude* of L_i , since this controls the per-factor term $L_i \delta_i$ in the tube radius of Theorem 2; we measure L_1, L_2 directly in Table 8.

A.3 Identifiability via factor dropout

The decomposition $s_{\text{comp}} = s + \sum_i \Delta_i$ (Definition 1) is not uniquely determined by training data alone. For any constants $c_i \in \mathbb{R}$ with $\sum_i c_i = 0$, the substitution $\tilde{s} := s + \sum_i c_i$, $\tilde{\Delta}_i := \Delta_i - c_i$, leaves the composed score $s + \sum_i \Delta_i$ unchanged but redistributes mass between the unconditional baseline and the per-factor corrections. Without an additional constraint, a learned s_θ could absorb arbitrary content into s that ought to live in Δ_i , in which case Theorem 1’s $2\sqrt{GM}$ bound on the true compositional gap would not transfer to s_θ^{comp} .

Factor dropout pins the decomposition. We resolve this in training by independently replacing each factor conditioning z_i with a learned null token \emptyset_i with probability p_{drop} , so that during training the network sees all 2^K subsets of factors. The unconditional score $s_\theta(\cdot, \emptyset_1, \dots, \emptyset_K)$ is then trained to match the score of $p(a | o)$ marginalized over all factors (the all-null behavior), and each single-factor score $s_\theta(\cdot, \emptyset_1, \dots, z_i, \dots, \emptyset_K)$ is trained to match the score of $p(a | o, z_i)$, marginalized over the others. This pins both s and each $\Delta_i = s(\cdot, z_i) - s(\cdot)$ to their information-theoretic targets and removes the constant ambiguity above. The dropout probability p_{drop} plays the same role as in classifier-free guidance (Ho and Salimans, 2022); we use $p_{\text{drop}} = 0.1$ throughout. Without factor dropout, the per-factor corrections Δ_i measured from s_θ are not the targets to which Theorem 1 applies, and the $2\sqrt{GM}$ bound would not transfer to the learned model.

A.4 Proof of Lemma 1 (ODE sensitivity)

Lemma (ODE sensitivity, Lemma 1 restated). *Let $s, s' : \mathcal{A} \times [0, \sigma_{\text{max}}] \rightarrow \mathcal{A}$ be two score fields with (a) $\|s - s'\|_\infty \leq \varepsilon$ and (b) s Lipschitz in its first argument with rate $L_a(\sigma)$. Let $\{a_\sigma\}, \{a'_\sigma\}$ be denoising paths generated by the reverse ODE (4) from a shared initial noise $a_{\sigma_{\text{max}}} = a'_{\sigma_{\text{max}}}$. Then $\|a_0 - a'_0\| \leq C_{\text{ode}} \varepsilon$, with C_{ode} given by (5).*

Proof. Define the error along the denoising path: $e(\sigma) = a_\sigma - a'_\sigma$. By the shared initial noise, $e(\sigma_{\text{max}}) = 0$. The reverse ODE (4) gives

$$\frac{de}{d\sigma} = f_{\text{dr}}(\sigma) e(\sigma) + \tilde{g}(\sigma) [s(a_\sigma, \sigma) - s'(a'_\sigma, \sigma)].$$

Split the score difference:

$$s(a_\sigma, \sigma) - s'(a'_\sigma, \sigma) = \underbrace{[s(a_\sigma, \sigma) - s(a'_\sigma, \sigma)]}_{\text{same field, different points: } \leq L_a(\sigma) \|e\|} + \underbrace{[s(a'_\sigma, \sigma) - s'(a'_\sigma, \sigma)]}_{\text{different fields, same point: } \leq \varepsilon}.$$

Setting $\mu(\sigma) = |f_{\text{dr}}(\sigma)| + |\tilde{g}(\sigma)| L_a(\sigma)$:

$$\left\| \frac{de}{d\sigma} \right\| \leq \mu(\sigma) \|e\| + |\tilde{g}(\sigma)| \varepsilon.$$

This is a linear differential inequality with forcing term, integrated backward from σ_{\max} (where $\|e\| = 0$) to $\sigma = 0$. Grönwall's inequality gives

$$\|e(\sigma)\| \leq \int_\sigma^{\sigma_{\max}} |\tilde{g}(\sigma')| \varepsilon \exp\left(\int_\sigma^{\sigma'} \mu(\sigma'') d\sigma''\right) d\sigma'.$$

Evaluating at $\sigma = 0$ yields $\|a_0 - a'_0\| = \|e(0)\| \leq C_{\text{ode}} \cdot \varepsilon$. \square

Remark 1. Unlike the standard Grönwall setting (same ODE, different initial conditions), here both denoising paths start from the *same* initial noise ($e(0) = 0$). The divergence is driven entirely by the score-field mismatch ε , which enters as a forcing term. The Lipschitz constant L_a then amplifies this forcing through feedback: the two paths drift apart, causing the *same* score field to evaluate differently at the two locations, which further increases the drift. The exponential in C_{ode} (5) reflects this feedback amplification.

A.5 Path-dependent LTV sensitivity (Lemma 2)

DDIM linearization. Discretize the reverse ODE (4) with K DDIM steps. Let \bar{a}_k ($k = 0, 1, \dots, K$) be the nominal denoising trajectory from a^* at noise levels $\sigma_0 = \sigma_{\max} > \sigma_1 > \dots > \sigma_K = 0$. Each step is

$$a_{k+1} = c_1(k) a_k + c_2(k) \hat{\varepsilon}_\theta(a_k, \sigma_k), \quad (13)$$

where c_1, c_2 are scheduler-determined coefficients (for DDIM: $c_1(k) = \sqrt{\bar{\alpha}_{k+1}/\bar{\alpha}_k}$, $c_2(k) = \sqrt{1 - \bar{\alpha}_{k+1}} - \sqrt{\bar{\alpha}_{k+1}(1 - \bar{\alpha}_k)/\bar{\alpha}_k}$, in the notation of Song et al. (2021a)). The eps-prediction $\hat{\varepsilon}_\theta$ and the score s are related by $\hat{\varepsilon}_\theta(x, \sigma) = -\sqrt{1 - \bar{\alpha}_\sigma} s(x, \sigma)$, so the score-mismatch hypothesis $\|s - s'\|_\infty \leq \varepsilon$ of Lemma 1 transfers to $\|\hat{\varepsilon}_\theta - \hat{\varepsilon}'_\theta\|_\infty \leq \varepsilon$ (since $\sqrt{1 - \bar{\alpha}_\sigma} \leq 1$). We state and measure the LTV bound below in $\hat{\varepsilon}_\theta$ -form throughout, matching standard DDIM implementations. Linearizing around the nominal yields per-step Jacobians

$$M_k = c_1(k) I + c_2(k) J_k, \quad J_k := \partial \hat{\varepsilon}_\theta / \partial a|_{\bar{a}_k, \sigma_k}, \quad (14)$$

and the discrete state-transition matrix from step k to K is

$$\Phi_{k,K} := M_{K-1} M_{K-2} \dots M_k, \quad \Phi_{K,K} := I. \quad (15)$$

Lemma 2 (Path-dependent LTV sensitivity). *Under the assumptions of Lemma 1 and the shared-seed condition $a_{\sigma_{\max}} = a'_{\sigma_{\max}} = a^*$, and to first order in ε along the nominal path $\{\bar{a}_k\}_{k=0}^K$,*

$$\|a_K - a'_K\| \leq C_{\text{ode}}^{\text{LTV}}(\bar{a}) \varepsilon + O(\varepsilon^2), \quad C_{\text{ode}}^{\text{LTV}}(\bar{a}) = \sum_{k=0}^{K-1} |c_2(k)| \|\Phi_{k+1,K}\|_2. \quad (16)$$

(*Indexing convention.*) The K reverse-sampling steps are indexed so that $k = 0$ is the noisy start ($\sigma_0 = \sigma_{\max}$) and $k = K$ is the clean end ($\sigma_K = 0$), matching the order in which DDIM evaluates them. The clean-end action error $\|a_K - a'_K\|$ in this lemma therefore corresponds to $\|a_0 - a'_0\|$ in the continuous-time Lemma 1, where $a_0 = a_{\sigma=0}$ is the clean action by the standard convention.

Proof. Let $e_k := a_k - a'_k$, so $e_0 = 0$ by the shared initial condition. Define the per-step eps-prediction forcing $\Delta \hat{\varepsilon}_k := \hat{\varepsilon}_\theta(a'_k, \sigma_k) - \hat{\varepsilon}'_\theta(a'_k, \sigma_k)$ and $b_k := c_2(k) \Delta \hat{\varepsilon}_k$; via the bridge $\hat{\varepsilon}_\theta = -\sqrt{1 - \bar{\alpha}_\sigma} s$,

the score-field mismatch assumption $\|s - s'\| \leq \varepsilon$ gives $\|\Delta\hat{e}_k\| \leq \sqrt{1 - \bar{\alpha}_k} \varepsilon \leq \varepsilon$, and hence $\|b_k\| \leq |c_2(k)| \varepsilon$.

$$\begin{aligned}
e_{k+1} &= M_k e_k + b_k + O(\|e_k\|^2) && \text{[linearize (13) around } \bar{a}_k\text{]} \\
e_K &= \sum_{k=0}^{K-1} \Phi_{k+1,K} b_k + O(\varepsilon^2) && \text{[discrete variation of constants from } e_0 = 0; \\
&&& b_k = O(\varepsilon) \text{ absorbs the nonlinear remainder]} \\
\|e_K\| &\leq \sum_{k=0}^{K-1} \|\Phi_{k+1,K}\|_2 \|b_k\| + O(\varepsilon^2) && \text{[triangle inequality, then submultiplicativity of } \|\cdot\|_2\text{]} \\
&\leq \sum_{k=0}^{K-1} |c_2(k)| \|\Phi_{k+1,K}\|_2 \varepsilon + O(\varepsilon^2) && \text{[apply } \|b_k\| \leq |c_2(k)| \varepsilon\text{].}
\end{aligned}$$

□

Remark 2 (Grönwall as a further relaxation). Applying the submultiplicativity inequality $\|\Phi_{k+1,K}\|_2 \leq \prod_{j=k+1}^{K-1} \|M_j\|_2$ in (16) together with the triangle inequality $\|M_j\|_2 \leq |c_1(j)| + |c_2(j)| L_a(\sigma_j)$ yields the discrete analog of the continuous Grönwall bound in Lemma 1; passing to the continuous-time limit recovers $C_{\text{ode}}^{\text{ana}}$ in (5) exactly. Hence $C_{\text{ode}}^{\text{LTV}}(\bar{a}) \leq C_{\text{ode}}^{\text{ana}}$, with strict inequality when (i) inter-step cancellation occurs (matrix product tighter than product of norms) and (ii) Jacobian structure is not captured by the scalar Lipschitz constant (discrete σ_{max} tighter than $L_a(\sigma_j)$). Both effects are typically present: Section 4.1 reports $C_{\text{ode}}^{\text{ana}} \approx 10^5\text{--}10^6$ (vacuous) versus $C_{\text{ode}}^{\text{LTV}} \approx 2\text{--}10$ on the $K = 50$ DDIM chain of our factored model — five to six orders of magnitude tighter.

Remark 3 (Remaining gap: nonlinear manifold contraction). Lemma 2 is a linearized worst-case bound: it (i) drops the $O(\varepsilon^2)$ Taylor remainder and (ii) assumes the score-error direction Δs_k aligns with $\Phi_{k+1,K}$'s top singular direction at every step. The linearization drop is an unavoidable feature of any sensitivity analysis; it is controlled as long as $\varepsilon \cdot C_{\text{ode}}^{\text{LTV}}$ remains small compared to the local radius of linearization. The direction-alignment assumption is *conservative*: empirically, Δs_k does not align with $\Phi_{k+1,K}$'s worst direction across steps, and the bound overestimates the measured action gap by a factor of order $10^1\text{--}10^2$ (Section 4.1). Closing this gap would require either distributional assumptions on Δs_k (stochastic Grönwall) or an analysis that exploits the *manifold-contractive* character of the learned score field: empirically, the denoising ODE is more contractive along the data manifold than its Jacobian predicts, because the score field itself points back toward the data manifold. Neither refinement is pursued in this paper; we report $C_{\text{ode}}^{\text{LTV}}$ as the best worst-case bound achievable by norm-based path analysis and separately report the empirical amplification in Section 4.1.

A.6 Proof of Theorem 1 (decomposition error bound)

Theorem (Decomposition error bound, Theorem 1 restated). *Suppose Assumption 1 holds and for every $\sigma \in [0, \sigma_{\text{max}}]$, the interaction log-ratio g_σ (2) is twice differentiable in a_σ with $\|\nabla_{a_\sigma}^2 g_\sigma(z, a_\sigma, o)\|_{\text{op}} \leq M$ uniformly in σ, a_σ, o, z . Then $\|s(a_\sigma, \sigma, o, z) - s_{\text{comp}}(a_\sigma, \sigma, o, z)\| \leq 2\sqrt{GM}$ for all a_σ, σ, o , and $z = (z_1, \dots, z_K)$.*

Proof. Step 1 (gradient bound on g_σ). Fix $\sigma \in [0, \sigma_{\text{max}}]$ and (z, a_σ, o) ; let $u := \nabla_{a_\sigma} g_\sigma(z, a_\sigma, o)$; assume $\|u\| > 0$ (the bound is trivial otherwise). With $v := u/\|u\|$ and the slice $\phi(t) := g_\sigma(z, a_\sigma + tv, o)$,

$$\begin{aligned}
\phi(t) &= \phi(0) + t\phi'(0) + \int_0^t (t-s)\phi''(s) ds && \text{[Taylor, integral remainder]} \\
&\geq \phi(0) + t\|u\| - \frac{1}{2}Mt^2 && \text{[} \|\phi''\| \leq M; \phi'(0) = \|u\|\text{]} \\
&\geq -G + t\|u\| - \frac{1}{2}Mt^2. && \text{[} \|\phi(0)\| \leq G \text{ by Assumption 1]}
\end{aligned}$$

Since $\phi(t) \leq G$ as well, $\|u\| \leq 2G/t + Mt/2$ for every $t > 0$; minimizing at $t^* = 2\sqrt{G/M}$ gives $\|\nabla_{a_\sigma} g_\sigma(z, a_\sigma, o)\| \leq 2\sqrt{GM}$ uniformly in σ, z, a_σ, o .

Step 2 (score decomposition identity). For all (a_σ, σ, o, z) , suppress these arguments with (\cdot) for brevity. For any conditioning variable c , Bayes' rule gives $p_\sigma(a_\sigma | o, c) = p_\sigma(a_\sigma | o) \cdot p_\sigma(c | a_\sigma, o) / p_\sigma(c | o)$. Since $p_\sigma(c | o)$ does not depend on a_σ , taking $\nabla_{a_\sigma} \log$ yields the score decomposition identity

$$s(\cdot, c) = s(\cdot) + \nabla_{a_\sigma} \log p_\sigma(c | a_\sigma, o). \quad (17)$$

Then:

$$\begin{aligned} s(\cdot, z) - s_{\text{comp}} &= [s(\cdot) + \nabla_{a_\sigma} \log p_\sigma(z | a_\sigma, o)] - s_{\text{comp}} && \text{[(17) with } c = z] \\ &= \nabla_{a_\sigma} \log p_\sigma(z | a_\sigma, o) - \sum_{i=1}^K \Delta_i && \text{[Def. 1; cancel } s(\cdot)] \\ &= \nabla_{a_\sigma} \log p_\sigma(z | a_\sigma, o) - \sum_{i=1}^K \nabla_{a_\sigma} \log p_\sigma(z_i | a_\sigma, o) && \text{[Def. 1; (17) with } c = z_i] \\ &= \nabla_{a_\sigma} g_\sigma(z, a_\sigma, o). && \text{[interaction log-ratio (2), at noise level } \sigma] \end{aligned}$$

Taking norms and applying Step 1, $\|s(\cdot, z) - s_{\text{comp}}\| = \|\nabla_{a_\sigma} g_\sigma(z, a_\sigma, o)\| \leq 2\sqrt{GM}$. \square

Remark 4 (Lifting the bounded-interaction assumption to noise levels). Assumption 1 and Theorem 1's curvature condition are stated on the noised log-ratio g_σ because the proof above invokes Bayes' rule on p_σ and reads the gap $s(\cdot, z) - s_{\text{comp}}$ as $\nabla_{a_\sigma} g_\sigma$ at every noise level the reverse ODE traverses. A clean-action bound $|g_0| \leq G$ does not in general imply $|g_\sigma| \leq G$ for $\sigma > 0$: Gaussian convolution alters the conditional densities $p_\sigma(z | a_\sigma, o)$ relative to $p(z | a, o)$, and g_σ interpolates between g_0 (at $\sigma \rightarrow 0$) and a fully marginalized log-ratio over observations alone (at $\sigma \rightarrow \sigma_{\text{max}}$, where action information is washed out). Two grounds for why the lifted bound is realistic in our setting:

(i) Closed form for deterministic experts. Section 3.3 establishes $p(a_0 | o, z) = \delta(a_0 - a_0^*(o, z))$, so $p_\sigma(a_\sigma | o, z) = \mathcal{N}(\alpha_\sigma a_0^*(o, z), \sigma^2 I)$ and the noised posterior $p_\sigma(z | a_\sigma, o)$ is a softmax over Gaussian likelihoods centered at the per-task expert actions $\{\alpha_\sigma a_0^*(o, z)\}_z$. The log-ratio g_σ then has a closed form, and uniform boundedness in σ reduces to a finite-diameter condition on the expert-action set $\{a_0^*(o, z) : z \in \prod_i \mathcal{Z}_i\}$ for each o — a standing requirement of bounded-action policies.

(ii) Empirical confirmation. The decomposition error $\varepsilon_D = \|s_{\text{joint}} - s_{\text{comp}}\|$ measured in Table 8 (mean 1.70, max 6.44) is by construction an empirical upper bound on $2\sqrt{GM}$ at the actual noised (a_σ, σ, o) encountered during sampling. A finite, small ε_D is direct evidence that the lifted assumption holds for the trained model on its operating distribution.

A.7 Proof of Theorem 2 (factored tube)

Theorem (Factored trajectory tube, Theorem 2 restated). *Under Assumptions 1, 3, and 2, and either the scalar Lipschitz condition $L_a(\sigma)$ of Lemma 1 (hypothesis (a)) or the path-Jacobian regularity of Lemma 2 under the shared-seed condition $a_{\sigma_{\text{max}}} = a'_{\sigma_{\text{max}}} = a^*$ (hypothesis (b)), the closed-loop state error satisfies the trajectory-tube bound (10) with $\varepsilon_s \leq 2\sqrt{GM} + (2K - 1)\eta + \sum_{i=1}^K L_i \delta_i$.*

Proof. Define $e_t = x_t - x_t^{\text{nom}}$.

Step 1 (score perturbation). The gap between the true joint score at the nominal factors and the composed learned score at the perturbed factors decomposes via three triangle-inequality steps, routed through the composed scores at the nominal task z^{nom} so that Assumption 3 is invoked on the trained network rather than on the unlearned true score:

$$\begin{aligned} &\|s(\cdot, z^{\text{nom}}) - s_\theta^{\text{comp}}(\cdot, z)\| \\ &\leq \underbrace{\|s(\cdot, z^{\text{nom}}) - s^{\text{comp}}(\cdot, z^{\text{nom}})\|}_{\leq 2\sqrt{GM} \text{ (Thm 1)}} + \underbrace{\|s^{\text{comp}}(\cdot, z^{\text{nom}}) - s_\theta^{\text{comp}}(\cdot, z^{\text{nom}})\|}_{\leq (2K-1)\eta \text{ (equation 9)}} + \underbrace{\|s_\theta^{\text{comp}}(\cdot, z^{\text{nom}}) - s_\theta^{\text{comp}}(\cdot, z)\|}_{\leq \sum_i L_i \delta_i \text{ (Asm 3)}}. \end{aligned}$$

The third term expands as $s_\theta^{\text{comp}}(\cdot, z^{\text{nom}}) - s_\theta^{\text{comp}}(\cdot, z) = \sum_{i=1}^K [s_\theta(\cdot, z_i^{\text{nom}}) - s_\theta(\cdot, z_i)]$ because both composed scores share the unconditional baseline $s_\theta(\cdot)$; Assumption 3 on each per-factor branch

then gives $\|s_\theta(\cdot, z_i^{\text{nom}}) - s_\theta(\cdot, z_i)\| \leq L_i \|z_i^{\text{nom}} - z_i\| \leq L_i \delta_i$, and the triangle inequality yields the displayed bound. Hence $\varepsilon_s \leq 2\sqrt{GM} + (2K - 1)\eta + \sum_i L_i \delta_i$.

Step 2 (action perturbation). Under hypothesis (a), Lemma 1 gives $\|a_t - a_t^{\text{nom}}\| \leq C_{\text{ode}}^{\text{ana}} \varepsilon_s$ uniformly over tasks. Under hypothesis (b), Lemma 2 gives the tighter per-task bound $\|a_t - a_t^{\text{nom}}\| \leq C_{\text{ode}}^{\text{LTV}}(\bar{a}^{(z)}) \varepsilon_s + O(\varepsilon_s^2)$ along the nominal denoising trajectory $\bar{a}^{(z)}$ (the $O(\varepsilon_s^2)$ remainder inherited from Lemma 2’s discrete linearization is controlled by Remark 3).

Step 3 (contraction). From (11) with $d = B_{\kappa} C_{\text{ode}} \varepsilon_s + w$: $\|e_{t+1}\| \leq \lambda \|e_t\| + d$. Unrolling: $\|e_t\| \leq \lambda^t \delta_0 + d/(1 - \lambda)$ (under hypothesis (b), the $O(\varepsilon_s^2)$ from Step 2 propagates additively through the per-step disturbance and the unrolled bound carries an $O(\varepsilon_s^2)$ correction in the steady-state term). \square

B Full-Race Experiments — Detailed Results

This appendix collects the per-task numbers, ablations, and certificate diagnostics behind the headline §4.1 results. Subsections are organized roughly in the order of the main-text claims: tracks and reference speeds (§B.2), per-task and per-track outcomes (§B.3), the composed-vs-joint comparison (§B.4), score-field diagnostics (§B.5), the K -network baseline’s training pipeline (§B.6), the DDIM step sweep (§B.7), the path-dependent LTV bound (§§B.8–B.10), and the 10-seed robustness study (§B.11) and residual-gap diagnostic (§B.12).

B.1 Training hyperparameters and compute

Both the state-based full-race policy (Section 4.1) and the vision-based single-gate policy (Section 4.2) share a common training recipe except where noted. Diffusion uses a DDPM cosine schedule with 100 noise steps for training and 50-step DDIM at inference, AdamW with learning rate 10^{-4} , batch size 32, and 1500 epochs. All training and evaluation runs use a workstation with one NVIDIA GeForce RTX 4080 SUPER (16 GB VRAM), an AMD Ryzen 9 7900X CPU (12 cores, 24 threads), and 64 GB system RAM, running CUDA 12.1 with PyTorch 2.4.1. Wall-clock time: state-based training is ~ 30 min per model; vision-based training runs ~ 2 h per DAGger round and ~ 50 epochs total; the 12-network composition baseline of Section 4.1 (Appendix B.6) totals ~ 40 min across all networks. All path-Jacobian and seed-sweep certificate measurements (Tables 10 and 12) run on the same single GPU.

B.2 Race tracks and reference speed profiles

The eight race tracks share a common gate layout. Maximum feasible speeds are determined by binary search: for each candidate speed, the SE(3) expert flies the cubic-spline reference and every gate is checked for passage with the actual half-width $r(z_2)$. A combination is declared infeasible if no candidate speed (down to a small lower bound) clears every gate.

Table 3: Race tracks and maximum feasible speeds (m/s). “—” indicates infeasible at that gate size.

Track	Gates	Narrow	Standard	Wide	Description
race1	8	—	2.1	2.4	Complex, U-turns
race2	9	—	2.1	2.4	Corkscrew
race3	7	—	2.1	2.5	Right-to-left sweep
race4	10	—	3.3	3.5	Long winding
race5	5	2.2	3.6	3.9	Short loop
race6	3	2.3	4.1	4.6	Simple run
race7	2	8.2	10.0	10.0	Height change
race8	2	7.0	7.9	7.9	U-turn

The full task space has $8 \times 3 = 24$ tasks; 20 are feasible. Races 1–4 with narrow gates exceed the SE(3) controller’s tracking precision and are omitted. Race 6 has the strongest gate-size speed differentiation ($2.0\times$ ratio between narrow and wide); races 7–8 are nearly speed-saturated, so the wide and standard maxima coincide.

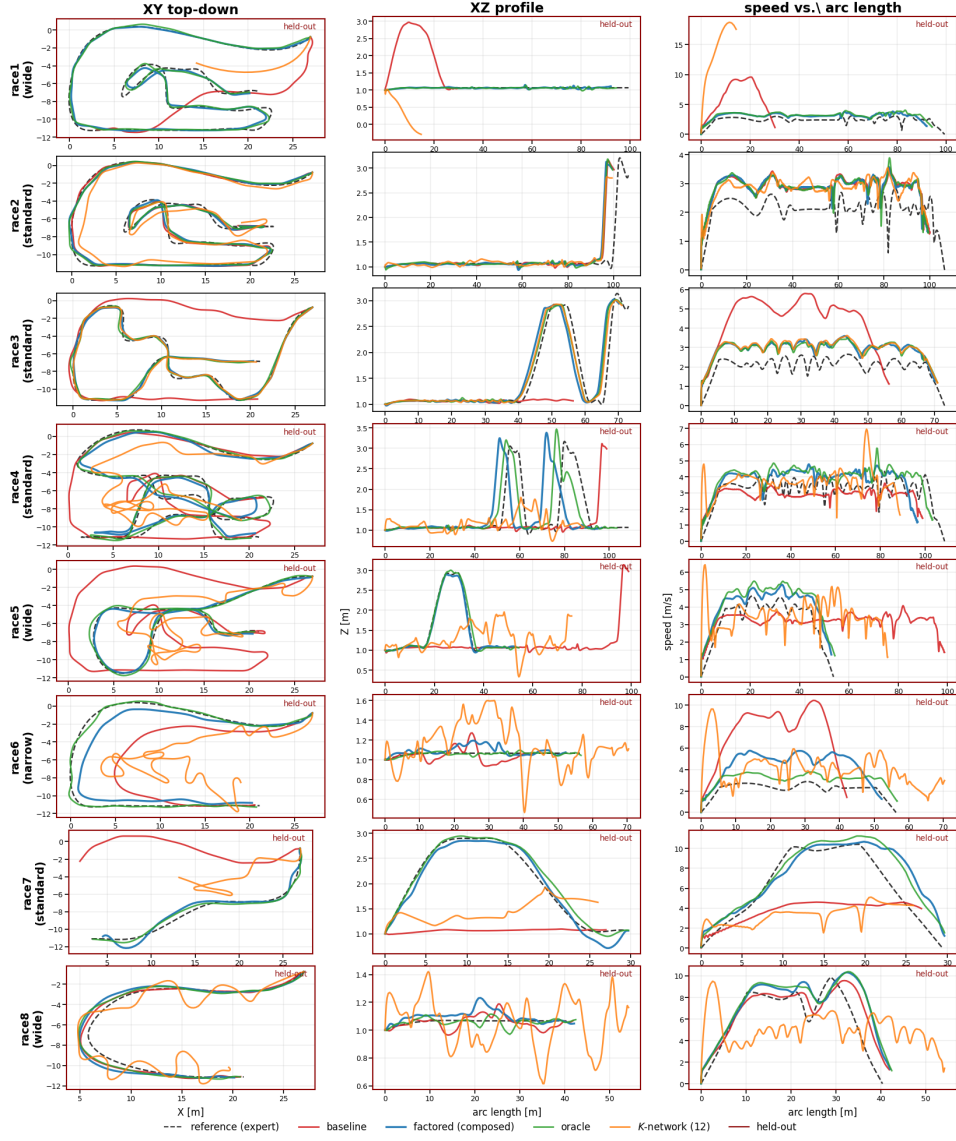


Figure 3: **Per-race closed-loop trajectories with all five methods overlaid.** One row per track; columns are XY top-down (geometric route), XZ side profile (height), and speed vs. arc length. For each race we pick the held-out joint pair where one exists (red border, “held-out” badge), else *standard* (race2, race3 have no held-out combo). Methods: expert reference (dashed black), baseline (red), factored composed (blue, ours), oracle (green), and the K -network composition baseline (orange). The factored policy tracks reference and oracle within ~ 0.1 m on every held-out row except (race6, narrow) — the lone composition failure where $\varepsilon_D \approx L_2$ (Table 8). The baseline collapses on every held-out task; the K -network composition produces erratic geometry and noisy speed profiles even on training tasks (race4_standard, race8_wide), corroborating Table 1.

B.3 Per-task and per-track results

Held-out task detail. Table 4 reports per-task gate passage on the six held-out (track, gate-size) pairs at $N = 50$. Pass/fail outcomes are invariant across the five DDIM seeds tested: different seeds produce different DDIM-generated reference trajectories, and the deterministic SE(3) controller plus plant tracks each one to a different state trajectory, but the trajectory variance across seeds stays within the gate’s pass/fail margin in every case — evidence of robustness, not of upstream determinism.

Table 4: Held-out tasks (5 seeds, $\sigma = 0\%$). Generated mean speed vs. reference from the speed map.

Track	Size	Gate passage		Speed [m/s]	
		Factored	Oracle	Gen.	Ref.
race1	wide	100%	100%	2.2	2.5
race4	std	100%	100%	3.0	3.4
race5	wide	100%	100%	3.0	4.0
race6	nar	0%	0%	3.4	2.4
race7	std	100%	100%	5.8	9.5
race8	wide	100%	100%	5.9	7.9
Total		5/6 (83%)	5/6		

Both factored and oracle achieve 100% on 5 of 6 held-out tasks. Both fail (race6, narrow): the trained policy generates 3.4 m/s for race6 (reference: 2.4 m/s), at the edge of the SE(3) controller’s ability to track slow speeds through race6’s geometry. Since oracle (trained directly on race6 narrow) also fails 0/3, the limit is a control / network-capacity constraint rather than a composition error; factored inherits the same constraint.

Speed fidelity. The gate-size score correction Δ_2 should produce monotonically increasing speeds as gate width increases. Table 5 confirms the ordering narrow < standard \leq wide on every track where narrow is feasible (with equality on race8, where standard and wide both generate 6.0 m/s). Generated speeds are conservative (below reference) but the relative ordering is always correct.

Table 5: Generated mean speed (m/s) by gate size (factored model). Reference in parentheses.

Track	Narrow	Standard	Wide
race1–5	—	2.0–3.0 (2.2–3.7)	2.3–3.3 (2.5–4.0)
race6	3.4 (2.4)	3.5 (4.2)	3.8 (4.8)
race7	5.0 (7.7)	5.8 (9.5)	6.1 (9.5)
race8	5.3 (7.0)	6.0 (7.9)	6.0 (7.9)

Per-track breakdown. Table 6 shows gate passage for the factored model per (track, gate-size), with held-out tasks in *italic*. Wide-gate tasks all pass (46/46) and standard passes 45/46 (the lone race1 standard miss is the only training-task failure outside narrow). Narrow remains the bottleneck (7/12), with both training failures concentrated on race8 narrow at 7 m/s through 0.3 m gates — at the dynamic limit of the SE(3) controller. Held-out tasks with non-zero scores match training-task performance on the same track.

B.4 Composed vs. joint inference

The headline §4.1 numbers use *composed* inference, $s_{\text{comp}} = s_{\emptyset} + \Delta_1(z_1) + \Delta_2(z_2)$ (Definition 1, requiring 3 forward passes per DDIM step). An alternative is *joint* conditioning: pass both factor embeddings to the shared network in a single forward pass. Table 7 compares the two modes on the same factored model and the full 20-task evaluation.

Composed inference passes 1 more gate than joint (98 vs. 97), within one gate of the oracle’s 95%. The two modes produce nearly identical trajectories; the small gate-count difference arises from marginal speed variations that push individual gates across the pass/fail threshold. This validates the additive score decomposition: the per-factor corrections Δ_1 and Δ_2 , learned independently through factor dropout, combine to reproduce the joint score’s trajectory quality.

Table 6: Per-track gate passage (factored). *Italic* = held-out. “—” = infeasible.

Track	Narrow	Standard	Wide	Total
race1	—	7/8	8/8	15/16
race2	—	9/9	9/9	18/18
race3	—	7/7	7/7	14/14
race4	—	<i>10/10</i>	10/10	20/20
race5	5/5	5/5	5/5	15/15
race6	0/3	3/3	3/3	6/9
race7	2/2	2/2	2/2	6/6
race8	0/2	2/2	2/2	4/6
	7/12	45/46	46/46	98/104

Table 7: Composed vs. joint inference (factored model, all 20 feasible tasks).

Inference	Gates	Rate	Error [m]
Joint ($s(z_1, z_2)$ directly)	97/104	93%	0.20
Composed ($s_{\emptyset} + \Delta_1 + \Delta_2$)	98/104	94%	0.23

B.5 Decomposition and Lipschitz diagnostics

Theorem 1 bounds the decomposition gap by $\|s_{\text{joint}} - s_{\text{comp}}\| \leq 2\sqrt{GM}$, where G bounds the pointwise interaction log-ratio and M bounds the score Hessian. Rather than estimating G and M separately, we directly measure the left-hand side: the decomposition error $\varepsilon_D := \|s_{\text{joint}} - s_{\text{comp}}\|$ on random (action, timestep) pairs across all training tasks. This provides an empirical upper bound on $2\sqrt{GM}$.

Table 8: Empirical decomposition error ε_D and per-factor Lipschitz constants L_1, L_2 . All values are ℓ_2 norms of score differences over random noise samples.

Quantity	Mean	95th pctl	Max
$\varepsilon_D = \ s_{\text{joint}} - s_{\text{comp}}\ $	1.70	4.23	6.44
L_1 (track, $\ s(z_1) - s(z'_1)\ $)	7.02	14.43	18.63
L_2 (gate-size, $\ s(z_2) - s(z'_2)\ $)	1.31	3.59	4.61

Key ratios:

- $L_1/L_2 = 5.4\times$: changing the track perturbs the score $5.4\times$ more than changing the gate size, confirming the heterogeneous sensitivity that makes the factored bound tighter than the joint bound (Appendix D).
- $\varepsilon_D/L_1 = 0.24$: the decomposition error is 24% of the dominant factor’s sensitivity — non-negligible but small enough that composition works on 5 of 6 held-out tasks.
- $\varepsilon_D/L_2 = 1.30$: the decomposition error is comparable to the gate-size sensitivity. This explains the (race6, narrow) failure: when the interaction is as large as the weaker factor’s own correction, the composed score cannot accurately reproduce the joint score for that task.

B.6 K -network composition baseline

The K -network row of Table 1 reports a PoCo / Mao-style baseline (Wang et al., 2024; Mao et al., 2025) adapted to our factor decomposition: rather than null-token masking of one shared network, we train $K = 1 + 8 + 3 = 12$ separate unconditional networks — an unconditional ε_{\emptyset} on all 14 held-in tasks pooled, eight track-only networks $\{\varepsilon_{\text{track}_i}\}_{i=1}^8$ each on data with $z_1 = \text{race}_i$, and three gate-size-only networks $\{\varepsilon_{\text{gate}_j}\}_{j=1}^3$ each on data with $z_2 = \text{gate}_j$ — and compose at inference via

$$\varepsilon_{\text{comp}}^{K\text{-net}}(x, t; z_1, z_2) = \varepsilon_{\text{track}_{z_1}}(x, t) + \varepsilon_{\text{gate}_{z_2}}(x, t) - \varepsilon_{\emptyset}(x, t).$$

This is structurally identical to our shared-network composition (Definition 1); the only difference is that each ε_{\bullet} comes from a different network rather than from null-token masking of one shared

network. Architecture (4.3M-parameter ConvNet), epochs (1500), optimizer, DDIM steps, normalization stats, SE(3) controller, carrot tracker, and gate-passagage criterion are unchanged from the shared-network setup.

The result is a $30\times$ collapse on held-out tasks (3% vs. 90%, Table 1). The mechanism follows from the theory. In the shared-network approach, null-token dropout (Section 3.2) regularizes the network to learn per-factor score corrections Δ_i that are *additive-compatible*: the empirical decomposition error ε_D on a held-in noised expert state is 1.70 (Table 8), small enough that the composed score approximates the joint score within the certifiable tube of Theorem 2. Separately trained networks have no such regularization; each $\varepsilon_{\text{track}_i}, \varepsilon_{\text{gate}_j}, \varepsilon_{\emptyset}$ is the score of a different marginal, fit independently, with no incentive for additive compatibility. Their sum $\varepsilon_{\text{track}} + \varepsilon_{\text{gate}} - \varepsilon_{\emptyset}$ is not constrained to approximate any joint score and, off-distribution, drifts arbitrarily.

The training-task degradation (66% vs. 97%) confirms this mechanistically. Even on training tasks where the joint (z_1, z_2) pair was seen, the K -network’s composition does not reconstruct it, because no single network ever saw a (z_1, z_2) -conditioned target. In particular, tracks with only one feasible held-in gate size — race1_standard (0/8) and race4_wide (0/10) — have a per-track network that collapses onto its single training raceline, and the per-gate correction does not consistently steer it back to the right joint trajectory. The shared network avoids this because the factor embeddings live in a continuous space and the joint trajectories provide a learning signal that the per-factor corrections must collectively reproduce.

B.7 DDIM step sweep

The headline §4.1 numbers use $N = 50$ DDIM steps. The trajectory-tube bound of Theorem 2 is driven by C_{ode} (eq. (5)), the amplification of per-step score-field mismatch into clean-action error across the reverse ODE. Grönwall’s inequality yields the analytical upper bound $C_{\text{ode}} = \int |\tilde{g}| \exp(\int [|f_{\text{dr}}| + |\tilde{g}|L_a]) d\sigma$, which grows exponentially with the denoising path length. We additionally measure the *empirical* amplification $C_{\text{ode}}^{\text{emp}} = \|a_0^{\text{comp}} - a_0^{\text{joint}}\| / \max_t \|s^{\text{comp}}(x_t) - s^{\text{joint}}(x_t)\|$ on the held-out composition set. Sweeping the DDIM step count $N \in \{10, 20, 30, 50\}$ (Table 9) exposes two findings.

Table 9: DDIM step sweep with the $p = 0.1$ factored checkpoint. $R_{\text{ss}}^{\text{emp}}$ plugs $C_{\text{ode}}^{\text{emp}}$ into Corollary 1 with $B_{\kappa}=0.05, \lambda=0.9, w=0.01$ (closed-loop constants defaulted, pending measurement). “Tube max” is the observed $\max_t \|x_t^{\text{comp}} - x_t^{\text{joint}}\|$ across all training tasks.

N	Comp. all	Comp. held-out	Joint all	$C_{\text{ode}}^{\text{emp}}$	$R_{\text{ss}}^{\text{emp}}$ [m]	Tube max [m]
10	80%	40%	89%	0.395	3.14	7.17
20	78%	50%	94%	0.136	1.15	3.47
30	91%	83%	95%	0.109	0.93	2.67
50	94%	90%	93%	0.064	0.59	2.37

Finding 1: empirical C_{ode} decreases with N , opposite to the analytical Grönwall bound. The analytical C_{ode} grows monotonically with N because each additional step adds a factor $\exp(|\tilde{g}(\sigma)|L_a(\sigma))$ to the cumulative amplification, as a worst-case over adversarial score fields. Empirically, $C_{\text{ode}}^{\text{emp}}$ drops from 0.40 at $N = 10$ to 0.06 at $N = 50$. The two composed and joint denoising chains stay close: finer discretization gives per-step mismatches more opportunity to cancel along the reverse ODE rather than compound. The resulting empirical amplification is sub-unity, meaning the end-to-end keypoint deviation is *smaller* than the largest per-step score mismatch observed along the path. This sharply separates the certified (Grönwall) regime from the operating regime: the conservative assumption that a perturbation expands at rate L_a forever is never realized in a well-trained score model.

Finding 2: composed inference requires more denoising steps than joint. Joint gate passage on held-out tasks is largely flat (89–95%) across N , while composed passage collapses from 90% at $N = 50$ to 40% at $N = 10$. Composed inference evaluates three score fields per denoising step and sums them with cancellation: $s_{\text{comp}} = s_{\emptyset} + \Delta_1 + \Delta_2$. Each field carries approximation error bounded by κ (eq. (8)), and the composition’s 3κ bound (eq. (9)) is realized when the individual errors do not align. Coarse DDIM schedules make this error budget per step large enough that the

composed score drifts off-manifold before downstream steps can correct it. Joint inference has a single-pass error budget of κ and is correspondingly more robust to step count.

Operating point. We adopt $N = 50$ as the canonical operating point throughout the headline tables: composed passage is 94% overall and 90% on held-out tasks, with the empirical certificate radius $R_{\text{ss}}^{\text{emp}} = 0.59$ m comfortably below the wide (1.0 m) and standard (0.762 m) gate half-widths. $N = 30$ is a viable lighter-compute alternative (91% overall, 83% held-out, 90 network evaluations vs. 150 for $N = 50$ — a $1.7\times$ speed-up) when overall passage matters more than held-out passage. The empirical tube $\max_t \|x_t^{\text{comp}} - x_t^{\text{joint}}\| = 2.37$ m at $N = 50$ still exceeds $R_{\text{ss}}^{\text{emp}}$; this gap is tracked to the defaulted values of B_κ, λ, w , which should be measured directly on the closed-loop SE(3) plant before the certificate is reported as tight.

B.8 Path-dependent LTV bound

Path-dependent LTV certificate via backward Lyapunov. Lemma 2 replaces the scalar per-step amplification σ_k with the spectral norm of the actual state-transition matrix $\Phi_{k+1,K} = M_{K-1}M_{K-2}\cdots M_{k+1}$ formed along a deterministic nominal DDIM trajectory $\{\bar{a}_k\}_{k=0}^K$ initialized from a fixed canonical $a_{\sigma_{\text{max}}} = x^*$. We compute this via the backward Gramian recursion $P_K = I$, $P_k = M_k^\top P_{k+1} M_k$ and form

$$C_{\text{ode}}^{\text{LTV}}(\bar{a}) = \sum_{k=0}^{K-1} |c_2(k)| \sqrt{\|P_{k+1}\|_2} = \sum_{k=0}^{K-1} |c_2(k)| \|\Phi_{k+1,K}\|_2.$$

The Jacobians $J_k = \partial \varepsilon_\theta^{\text{comp}} / \partial x|_{\bar{a}_k, \sigma_k}$ are computed by `torch.func.jacrev` (128×128 ; state dimension 32×4). A backward matrix recursion in float64 maintains $\|P_k\|_2$ at each step; cross-checking against explicit Φ products agrees to machine precision ($\approx 10^{-15}$). Table 10 reports $C_{\text{ode}}^{\text{LTV}}(\bar{a}^{(z)})$ aggregated over task conditions z and seeds.

Table 10: Path-dependent LTV bound $C_{\text{ode}}^{\text{LTV}}$ at one canonical seed $x^* = \text{torch.randn}(\text{seed} = 0)$, aggregated over all 24 task combinations (18 training + 6 held-out, excluding 4 infeasible). Columns: mean, median, and max across combos at seed 0; the mean-across-seeds of the per-seed mean over combos (10 seeds) shows insensitivity to the canonical seed choice in the typical case. Last column: ratio to empirical $C_{\text{ode}}^{\text{emp}}$.

N	mean	median	max	$\overline{\text{mean}} \pm \text{std}$ (10 seeds)	$C^{\text{LTV}}/C^{\text{emp}}$
10	85.6	—	498	—	$110\times$
20	22.2	—	89	—	$61\times$
30	17.1	—	71	—	$53\times$
50	9.68	4.38	52.0	13.3 ± 4.6	$38\times$

Finding: the LTV bound tightens Grönwall by six orders of magnitude, but the remaining ~ 10 – $100\times$ gap to empirical amplification is not closable by norm-based analysis. At $N = 50$, for the representative combo `race3_standard`, $C_{\text{ode}}^{\text{LTV}} \approx 4.0$ versus $C_{\text{ode}}^{\text{ana}} \approx 8.4 \times 10^5$. The LTV bound varies across combos from 3.35 (best) to 52.1 (worst, dominated by held-out combos `race8_wide` and `race7_standard`); the gap to the empirical per-combo amplification (which ranges 0.195–0.299) is 13–17 \times on typical combos, widening to $\sim 170\times$ on the worst-case combo. The LTV bound exploits inter-step cancellation: successive Jacobians do not share their worst singular directions, and the true state-transition matrix $\|\Phi_{k+1,K}\|_2$ is correspondingly less amplifying than naive per-step worst-case products would suggest. A diagnostic decomposition of the residual gap between the LTV bound and the empirical amplification appears in §B.12; the looseness is nonlinear and directional and cannot be closed by any norm-based bound.

B.9 Per-combo ε_s tightening

The R_{ss} formula (??) depends on ε_s , the sup-bound on per-step score mismatch along the denoising path. A distribution-wide worst-case estimate yields $\varepsilon_s \approx 15.4$ for our model, which is $\sim 10\times$ larger than the actual maximum $\|\Delta\varepsilon_k\|$ encountered along any specific nominal. Under the deterministic-seed setup, the certificate is indexed by a fixed nominal trajectory $\bar{a}^{(z)}$, and the rigorous sup-bound

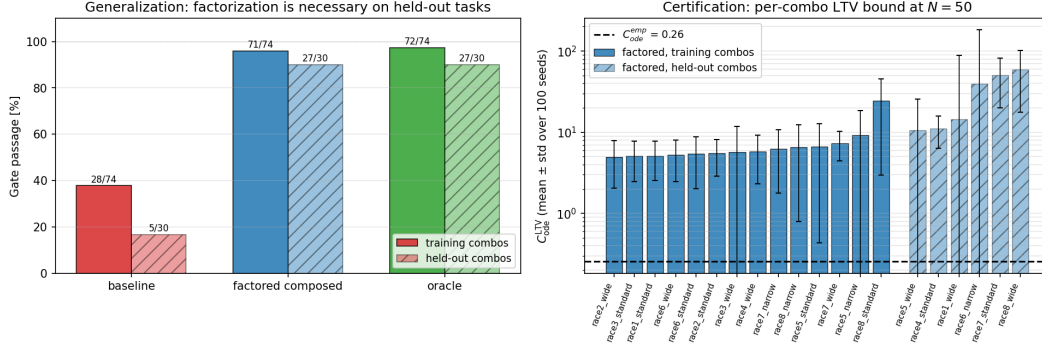


Figure 4: **Generalization (left) and certification (right) for the factored model at $N=50$.** Left: gate passage on training (solid) vs. held-out (hatched) tasks (same headline numbers as Table 1, plotted per task). Right: path-dependent C_{ode}^{LTV} per task, mean \pm std over 10 canonical seeds, sorted within each group. Training tasks cluster at $C \approx 5$ with low variance; held-out tasks have higher means and an order-of-magnitude wider seed spread, indicating that the certificate inherits the composed score’s extrapolation uncertainty. Empirical $C_{ode}^{emp} \approx 0.26$ shown as dashed reference.

$\varepsilon_s^{(z)} := \max_k \|\Delta \varepsilon_k^{(z)}\|$ need only hold along that trajectory. Table 11 shows the effect at $N = 50$: per-combo $\varepsilon_s^{(z)}$ ranges 1.20–2.06 (vs. default 15.4), and the resulting R_{ss} shrinks by the same factor of ~ 10 , moving typical combos from ~ 30 m to ~ 3 m without any change to the LTV certificate.

Table 11: Effect of replacing the default scalar $\varepsilon_s = 15.4$ with per-combo $\varepsilon_s^{(z)} = \max_k \|\Delta \varepsilon_k^{(z)}\|$ measured along the nominal at $N = 50$, seed 0. Both values are rigorous sup-bounds for the respective scope (distribution-wide vs. along-nominal). Gate half-widths: 0.3 m (narrow), 0.762 m (standard), 1.0 m (wide). Combo set is 20 tasks spanning 8 tracks \times 3 gate sizes.

	default	per-combo	ratio	closes gate
ε_s range	15.4	[1.20, 2.06]	$\sim 10\times$	—
R_{ss} (race3_std)	31.3 m	3.57 m	$\sim 10\times$	no
R_{ss} (best combo)	25.9 m	2.46 m	$\sim 10\times$	no
R_{ss} (worst combo)	207 m	17.0 m	$\sim 10\times$	no
# combos with $R_{ss} < \text{gate}$	0/20	0/20	—	—

None of the 20 tasks achieves rigorous R_{ss} below its gate half-width even under the tightened ε_s . The residual factor of ~ 13 between R_{ss} and the observed deployment tubes is the same nonlinear manifold contraction quantified in §B.12. We report this calculation to separate looseness that is addressable by careful measurement (ε_s : $10\times$ tightening here) from looseness that is structural to norm-based Lipschitz analysis (nonlinear manifold contraction: $\sim 10\times$, requires a different certificate).

B.10 Continuous-time limit

Running the backward-Lyapunov computation at $N \in \{100, 200\}$ (seed 0, all 20 combos) gives $C_{ode}^{LTV} = 5.60$ (mean over combos, min 1.95, max 29.1) at both N values, *identical to three decimal places*. The measured empirical amplification plateaus alongside: $C_{ode}^{emp} = 0.242$ (mean over combos) at $N=100$ versus 0.242 at $N=200$. Both have converged to the continuous-time probability-flow ODE limit; additional DDIM steps cannot tighten the bound or the observed amplification.

For race3_standard: C_{ode}^{LTV} drops from 4.04 at $N=50$ to 2.26 at $N=100$ and stays there; the corresponding empirical C_{ode}^{emp} goes $0.30 \rightarrow 0.27 \rightarrow 0.27$. The gap between certificate and empirical at the continuous-time limit is therefore $\sim 9\times$ for this combo, $\sim 23\times$ for the mean over combos, and $\sim 100\times$ for the worst combo. These are fundamental limits of norm-based path analysis on this trained score network; closing them requires either a training-side change (spectral regularization, rectified flow) or a non-norm-based certificate that captures manifold contraction.

B.11 Seed robustness of the LTV certificate

Because the deterministic-seed analysis commits the certificate to a specific canonical x^* , we measure how sensitive the numerical bound is to that choice via a 10-seed sweep at $N=50$. Table 12 reports per-combo $C_{\text{ode}}^{\text{LTV}}$ mean \pm std and coefficient of variation (CV). A sharp dichotomy emerges: training combos are seed-robust (CV 0.4–0.7, typical mean ≈ 5); held-out combos are fragile (CV up to 5.2, with occasional single-seed explosions to hundreds).

Table 12: Per-combo $C_{\text{ode}}^{\text{LTV}}$ across 10 canonical seeds at $N=50$. “Mean” is over 10 seeds for that combo; “CV” = std/mean. Held-out combos were not seen during training.

combo	mean	std	CV	type
<i>Training combos (14 shown, 14 total, sorted by mean):</i>				
race2_wide	4.97	2.91	0.59	train
race3_standard (ref.)	5.14	2.65	0.52	train
race1_standard	5.14	2.60	0.51	train
race6_wide	5.26	2.80	0.53	train
race6_standard	5.42	3.40	0.63	train
race2_standard	5.52	2.65	0.48	train
race3_wide	5.73	6.11	1.07	train
race4_wide	5.81	3.48	0.60	train
race7_narrow	6.24	4.46	0.72	train
race8_narrow	6.58	5.78	0.88	train
race5_standard	6.62	6.18	0.93	train
race7_wide	7.36	2.94	0.40	train
race5_narrow	9.21	9.43	1.02	train
race8_standard	24.39	21.44	0.88	train
<i>Held-out combos (6 total, sorted by mean):</i>				
race4_standard	11.15	4.80	0.43	held-out
race5_wide	10.52	14.94	1.42	held-out
race1_wide	14.45	74.59	5.16	held-out
race6_narrow	39.57	142.75	3.61	held-out
race7_standard	51.10	31.08	0.61	held-out
race8_wide	59.58	41.90	0.70	held-out

Finding 5: the LTV certificate is seed-robust on training combos but not on held-out combos.

Training combos give $C_{\text{ode}}^{\text{LTV}} = 6.8 \pm 4.9$ (mean across combos of per-combo means), with one outlier (race8_standard at 24.4). Held-out combos give $C_{\text{ode}}^{\text{LTV}}$ values an order of magnitude larger on average and CVs up to 5.2: certain seed-combo pairs drive $C_{\text{ode}}^{\text{LTV}}$ into the hundreds. Two operational consequences:

- A worst-case task-aggregate bound $\max_z C_{\text{ode}}^{\text{LTV}}(z)$, required for a certificate that covers all deployment conditions, is dominated by held-out outliers and does not reflect typical behavior.
- The gate-passage evidence (Section 4.1, 94% at $N=50$) shows held-out combos *do* pass the gate in closed-loop, despite their pathological certificate value. The certificate is conservative on held-out tasks, not wrong: the nonlinear manifold contraction absorbs what the worst-case bound over-predicts.

Future work could tighten the held-out certificate by either (i) increasing factor-dropout regularization during training to encourage flatter Jacobian spectra on unseen conditions, or (ii) training with rectified-flow / flow-matching objectives that explicitly straighten trajectories and reduce per-step Jacobian anisotropy.

B.12 Residual gap diagnostic

The LTV bound $C_{\text{ode}}^{\text{LTV}}$ still overestimates the empirical amplification by an order of magnitude. We decompose this residual along a nominal denoising path by comparing three quantities: the actual action gap, the *linearized* prediction $\|\sum_k c_2(k) \Phi_{k+1,K} \Delta \varepsilon_k\|$ that uses the measured per-step score errors $\Delta \varepsilon_k$ with their true directions, and the LTV bound $\sum_k |c_2(k)| \|\Phi_{k+1,K}\|_2 \|\Delta \varepsilon_k\|$ that replaces directional propagation with operator-norm worst case.

Table 13: Source-of-looseness decomposition at $N = 50$, seed 0, mean over 14 training tasks.

Quantity	Value [m]	Ratio to actual
actual $\ a_K^c - a_K^j\ $	0.095	1.0×
linearized $\ \sum_k c_2 \Phi \Delta \varepsilon\ $	0.562	5.9×
LTV bound $\sum_k c_2 \ \Phi\ \ \Delta \varepsilon\ $	0.938	9.9×

Two distinct effects show up. The $5.9\times$ linearization gap is *nonlinear manifold contraction*: the score field points back toward the data manifold and shrinks errors faster than its Jacobian predicts, an effect that no operator-norm analysis on J_k can capture. The further $\sim 2\times$ from linearized to LTV bound is *directional alignment*: the LTV bound assumes $\Delta \varepsilon_k$ aligns with each $\Phi_{k+1,K}$'s top singular direction, which empirically it does not. Closing either gap requires a non-norm-based tool: distributional assumptions on $\Delta \varepsilon_k$, or a certificate that explicitly represents manifold distance.

C Single-Gate Vision: Ablations

We report two ablations that corroborate the mechanism by which the factored architecture decomposes appearance from geometry in the single-gate vision setting (Section 4.2).

The venue embedding is doing useful work. Raising the venue null-token dropout from 0.1 to 0.4 hurts zero-shot pool by -3.4 pp on success rate and worsens crash rate by $+22.5$ pp. Replacing the trained venue embedding with the null token at evaluation ($vd=0.4 + null_venue\ eval$) degrades pool further to 22.5% success / 46.7% crash, showing that the venue row carries information even on a held-out venue. Weakening the venue embedding during training does not push the visual encoder toward distribution-invariant features; it degrades both in-distribution and zero-shot performance.

Backbone choice: DINO-v2 ViT-B with attention pooling. Replacing the fine-tuned ResNet-18 with a DINO-v2 ViT-B/14 backbone using attention pooling over 252 patch tokens, with the last transformer block fine-tuned, matches the ResNet-18 factored model on a different held-out venue (*Field*-holdout): 60.0% success on the three training venues vs. 35.8% zero-shot, with crash rate 19.2% and best validation loss 0.0522 (vs. 0.0608–0.0611 for the ResNet-18 factored / unfactored baselines on the same holdout). As a control, a *frozen* DINO-v2 ViT-S/14 backbone using only the cls token collapses both in-distribution and zero-shot (-19.2 pp success on pool, $+49.2$ pp crash relative to the fine-tuned ResNet-18): the cls token compresses away the spatial cues required for visual servoing, and a frozen backbone cannot adapt to gate localisation. The factored advantage is therefore not a backbone artefact: it persists when the visual encoder is swapped for a self-supervised ViT, provided enough capacity is left trainable for the encoder to acquire gate-localisation features.

D Factored vs. joint bound

A non-compositional approach that learns the joint score $s_\theta(\cdot, z)$ directly bounds the score perturbation by $L_{\text{joint}}\|\delta\|$, where L_{joint} is the Lipschitz constant over the product space $\mathcal{Z}_1 \times \dots \times \mathcal{Z}_K$ and $\|\delta\| = \sqrt{\sum_i \delta_i^2}$. The joint bound has no decomposition error, so the total score perturbation is $\varepsilon_s^{\text{joint}} \leq \eta + L_{\text{joint}}\|\delta\|$ (a single forward pass per inference, vs. $(2K - 1)\eta$ for the composed score below).

The factored bound replaces this with $\varepsilon_s^{\text{fact}} \leq 2\sqrt{GM} + (2K - 1)\eta + \sum_i L_i \delta_i$. By Cauchy–Schwarz, $\sum_i L_i \delta_i \leq \sqrt{\sum_i L_i^2} \|\delta\|$, with equality iff (L_1, \dots, L_K) and $(\delta_1, \dots, \delta_K)$ are linearly dependent ($L_i \propto \delta_i$). The gap is substantial when per-factor sensitivities are heterogeneous and δ is not aligned with the largest L_i directions. The joint Lipschitz constant is itself bounded *above* by the per-factor RMS, $L_{\text{joint}} \leq \sqrt{\sum_i L_i^2}$ (any two factor-product points are connected by a coordinate-axis path of combined length $\leq \sqrt{\sum_i L_i^2} \|\delta\|$). This inequality can be strict: for the identity map $f(z_1, z_2) = (z_1, z_2)$ on $\mathbb{R}^2 \rightarrow \mathbb{R}^2$, $L_1 = L_2 = 1$ gives $\sqrt{L_1^2 + L_2^2} = \sqrt{2}$, but the joint operator norm is $L_{\text{joint}} = 1$, so $\sqrt{\sum_i L_i^2} > L_{\text{joint}}$ strictly. Consequently both $\sum_i L_i \delta_i$ and $L_{\text{joint}}\|\delta\|$ are dominated by $\sqrt{\sum_i L_i^2} \|\delta\|$, but neither is uniformly tighter than the other; their relative size depends

on the alignment of δ with the Lipschitz directions of the two score fields. The factored certificate beats the joint certificate when the factored score perturbation is the smaller of the two:

$$2\sqrt{GM} + \sum_i L_i \delta_i < L_{\text{joint}} \|\delta\|,$$

a condition that depends on both the factor-interaction strength (G, M) and the alignment of δ with the dominant Lipschitz directions; it is not guaranteed by the structure alone. If the factor interaction is strong (G large) or the log-ratio is highly curved (M large), the decomposition cost dominates and the joint bound is tighter.

The *generalization* benefit of factorization (Theorem 1) is unconditional: it enables evaluation on unseen tasks where no joint model exists. The *certification* benefit is conditional: the factored tube is tighter than the joint tube only when the approximate conditional independence is strong enough ($2\sqrt{GM}$ small) and the per-factor weighting makes $\sum_i L_i \delta_i$ smaller than $L_{\text{joint}} \|\delta\|$.

E Extended Related Work

This appendix expands Section 5 with a per-method comparison of recent compositional-diffusion methods for control and a side-by-side summary table.

PoCo (Wang et al., 2024) merges K diffusion networks trained on different data sources (task / behavior / domain slices) via product-of-experts on noise predictions; the goal is fusing heterogeneous demonstration data, not generalizing to unseen factor combinations. Compose Your Policies (GPC) (Cao et al., 2026) takes test-time convex combinations of K pre-trained vision-language-action policies, with the weights set by task descriptors, and provides a per-step Grönwall-type improvement bound related to our Lemma 1; this composes whole policies rather than per-factor corrections of a shared one, and named factors are not part of the formalism. Factorized Diffusion Policy (FDP) (Liu et al., 2025) combines K expert U-Nets through a learned router; here “factor” means a latent behavioral mode discovered by clustering, not a named external attribute with known semantics. Modality-Composable DP (Cao et al., 2025) composes scores across visual modalities (RGB vs. point cloud), so the composition runs over input streams rather than task structure. Mao et al. (2025) compose track-specific diffusion planners for 2D FITENTH cars via weighted interpolation, which is one factor (track) realized with K separately trained networks.

We differ on four axes: (i) a single shared score network whose per-factor corrections are obtained by null-token dropout, rather than K separately trained networks plus a router or weighting scheme; (ii) named semantic factors indexing a product space, with demonstrated generalization to held-out factor combinations, rather than composition over latent modes, heterogeneous data sources, or whole policies; (iii) a formal trajectory-tube certificate that implies task-level gate passage, rather than a per-step action-error bound or an empirical collision rate; (iv) 3D racing-drone control rather than manipulation, autonomous driving, or 2D cars. The single shared-network realization matters beyond parameter count: per-factor null-token dropout is what makes the decomposition $s_{\text{comp}} = s_{\emptyset} + \sum_i \Delta_i$ identifiable from training data (Section 3.2), and it is this structure that enables the per-factor Lipschitz bounds L_i used in the certificate.

Table 14: Compositional diffusion for control: prior work vs. ours. *Factor type*: whole policies (W), latent modes (L), or named semantic factors (S). *Certificate*: single-step action-error bound (A), task-success guarantee (T), or none.

Method	Domain	Networks	Factor type	# factors	Certificate
PoCo (Wang et al., 2024)	Manipulation	K	W	3 (slices)	none
GPC (Cao et al., 2026)	Manipulation	K	W	K	A
FDP (Liu et al., 2025)	Manipulation	K + router	L	latent	none
Mod.-Comp. DP (Cao et al., 2025)	Manipulation	K	W	modalities	none
Mao et al. (2025)	2D racing	K	W	1 (track)	none
Ours	3D drone	1 shared	S	2	T

E.1 Certified robustness for neural-network controllers

Lipschitz-constant bounds (LipSDP, Fazlyab et al., 2019) compute global Lipschitz constants of feed-forward networks via semidefinite programming and certify outputs under bounded input perturbations. Reachability of neural-network controllers (ReachLP, Everett et al., 2021) propagates polytopic input sets through the controller step by step to bound reachable state sets. Black-box perception contracts (Astorga et al., 2023; Ji et al., 2025) treat the perception–control stack as one nonlinear map and establish input/output assumption pairs that imply task-level safety. All three frameworks bound output variation against the entire input variation at once. In our setting the input variation is structured as a product over named factors, and the per-factor decomposition $\sum_i L_i \delta_i$ replaces $L_{\text{joint}} \|\delta\|$ with a tighter sum whenever the per-factor sensitivities L_i differ.

E.2 Sequential skill composition

SkillDiffuser (Liang et al., 2024) and Generative Skill Chaining (Mishra et al., 2023) compose pre-trained skills as a sequence in time: the trajectory is partitioned into segments, each generated by a different skill, and the composition runs along the temporal axis. Our composition is orthogonal: a single denoising step produces actions conditioned on all K factors simultaneously, and the additive structure is across factor scores at each step rather than across time.

E.3 Champion-level drone racing systems

Champion-level autonomous drone racing systems (Kaufmann et al., 2023; Song et al., 2023; Foehn et al., 2021) achieve sub-second lap times on a fixed track via per-track training, model-predictive control with track-specific cost functions, or extensive simulation-to-real fine-tuning. These systems beat the factored policy on absolute lap time but require re-tuning for each new track and gate-size combination. We trade peak speed for sample-efficient cross-track generalization with a closed-loop certificate that holds across $\mathcal{Z}_1 \times \mathcal{Z}_2$.

E.4 Domain randomization and task-conditioned multi-task RL

Domain randomization (Tobin et al., 2017; Sadeghi and Levine, 2017) trains a policy on a randomized distribution over environments to encourage invariance. Task-conditioned multi-task RL conditions the policy on a task descriptor and pools trajectories across tasks during training. Both approaches condition or randomize over factors at training time without explicit per-factor composition; the unfactored baseline in Section 4 represents this regime within our setup and reaches only 17% on held-out gates, indicating that randomization or generic conditioning alone does not yield held-out compositional generalization in our benchmark.